MODELING 1/f NOISE IN a-Si:H FIELD-EFFECT TRANSISTORS

A Thesis Submitted to the College of

Graduate Studies and Research

in Partial Fulfillment of the Requirements

for the Degree of Master of Science

in the Department of Electrical and Computer Engineering

University of Saskatchewan

Saskatoon

By

Yang Xu

PERMISSION TO USE

In presenting this thesis in partial fulfilment of the requirements for a Postgraduate degree from the University of Saskatchewan, I agree that the Libraries of this University may make it freely available for inspection. I further agree that permission for copying of this thesis in any manner, in whole or in part, for scholarly purposes may be granted by the professor or professors who supervised my thesis work or, in their absence, by the Head of the Department or the Dean of the College in which my thesis work was done. It is understood that any copying or publication or use of this thesis or parts thereof for financial gain shall not be allowed without my written permission. It is also understood that due recognition shall be given to me and to the University of Saskatchewan in any scholarly use which may be made of any material in my thesis.

Requests for permission to copy or to make other use of material in this thesis in whole or part should be addressed to:

Head of the Department of Electrical and Computer Engineering

University of Saskatchewan

Saskatoon, Saskatchewan

Canada S7N 5A9

ABSTRACT

Hydrogenated amorphous silicon (a-Si:H) thin film transistors (TFTs) are used as switching elements in large area active matrix liquid crystal displays and various image sensing devices for radiation detection. The noise inherent in the a-Si:H TFTs contributes to the overall noise figure of such devices and degrades the signal to noise ratio; therefore, the noise is an important factor in the design of the devices. The noise of the a-Si:H TFTs has been studied experimentally, but the origin of the noise is not understood.

This work calculates the noise of the a-Si:H TFTs based on a simulation of operation of the TFTs and the hypothesis that the device noise is due to the intrinsic noise of the a-Si:H material. An a-Si:H TFT with an inverted-staggered structure has been simulated by numerically solving the fundamental transport equations for various gate and drain-source voltages. The drain-source curves derived from the simulation agree qualitatively with the experimental results: both the linear and saturated regions are observed. The low frequency noise was calculated based on the charge density distribution in the channel obtained from the simulation and the known dependence of the noise in the a-Si:H on the charge density, Hooge's relation. The calculated noise power increases with the drain-source voltage and is inversely proportional to the gate voltage or the effective channel length. The curves agree qualitatively with the experimental results. The calculated noise power agrees quantitatively with the experiments when the scaling parameter in Hooge's relation, α_H, is set to 1×10^{-3}. This value agrees with the experimentally determined value for a-Si:H. The results are consistent with the hypothesis that the low frequency noise in the a-Si:H TFTs is due to the material itself.

ACKNOWLEDGEMENTS

I would like to express my sincere gratitude to my supervisor, Dr. Robert Johanson, and co-supervisor, Dr. Safa O. Kasap, for giving me the opportunity to study in the material area. Especially, I like to thank Dr. Robert Johanson for his patience, support, advice and leadership throughout this project. I would not finish this project without his assistance and support. I would also like to thank all members of my research group; especially, Bud Fogal, Georgy Belev, Gokul Soundararajan, Hasibul Majid, Isha Dash, Kanghyun Kim, Sujata Panigrahi, Wee C Tan for their friendship and assistance. Finally, I would like to thank my parents and my friend Peng Xu, for their patience, encouragement and love.

TABLE OF CONTENTS

LIST OF FIGURES

LIST OF TABLES

LIST OF ABBREVIATIONS

a-Si:H	Hydrogenated amorphous silicon
AMA	Active matrix array
B	Bandwidth (Hz)
BCE	Back-channel-etched
C	Capacitance per unit area (F/m^2)
D_e	Electron diffusion constant (m^2s^{-1})
D_h	Hole diffusion constant (m^2s^{-1})
DOS	Density of states ($m^{-3}J^{-1}$)
E_C	Conduction energy (eV)
E_V	Valance energy (eV)
E_F	Fermi energy (eV)
ES	Etch-stopper
f	Frequency (Hz)
FEM	Finite element method
FETs	Field effect transistors
G_e	Generation rate (electrons) ($m^{-3}s^{-1}$)
G_h	Generation rate (holes) ($m^{-3}s^{-1}$)
GS	Gauss-Seidel method
h	Space between two points (m)
I_{DC}	DC current (A)
I_{ds}	Drain source current (A)
I_{rms}	rms current (A)
IGFETs	Insulated gate field effect transistors
JFETs	Junction field effect transistors
k	Boltzmann's constant (1.38×10^{-23} J/°K)

L	Channel length (m)
LCD	Liquid crystal display
MOSFET	Metal-oxide semiconductor FET
n	Electrons concentration (m^{-3})
n_f	Concentration of the mobile electrons (m^{-3})
N	Number of carriers (m^{-3})
N_D	Electron concentration per unit area at drain
N_A^-	Ionized acceptors (m^{-3})
N_D^+	Ionized donors (m^{-3})
N_S	Electron concentration per unit area at source
N_{total}	Total number of carriers (m^{-3})
p	Holes concentration (m^{-3})
p_f	Concentration of mobile holes (m^{-3})
P	Thermal noise power spectral density
q	Electronic charge (1.602×10^{-19} C)
R	Resistance (Ω)
R_e	Recombination rate (electrons) ($m^{-3}s^{-1}$)
R_h	Recombination rate (holes) ($m^{-3}s^{-1}$)
R_0	Mean resistance (Ω)
rms	Root mean square
S	Power spectral density (Hz^{-1})
S_n	Normalized current noise power density (Hz^{-1})
S_r	Power spectral density of resistance fluctuations (Hz^{-1})
SOR	Successive over-relaxation method
T	Temperature (K)
t_j	Random arrival times of the carriers (s)
TFTs	Thin film transistors
V	Voltage (V)

V_{ds}	Source-drain voltage (V)
V_g	Gate voltage (V)
V_{th}	Threshold voltage (V)
W	Channel width (m)
ω	Angular frequency (rad s^{-1})
α_H	Hooge's parameter
γ	Correlation coefficient
λ	Tunneling constant for electrons
μ_e	Mobility of electrons ($m^2V^{-1}s^{-1}$)
μ_h	Mobility of holes ($m^2V^{-1}s^{-1}$)
μ_{lat}	Mobility associated with lattice scattering
μ_{imp}	Mobility associated with impurity
τ	Delay time (s)
ν_0	Trap release frequency
ρ	Charge density (Cm^{-3})
$\vec{D}$	Displacement field
$\vec{E}$	Electric field ($V^{-1}m$)
ε	Permittivity of medium (Fm^{-1})
ε_0	Permittivity of free space (8.8542×10^{-12} $CV^{-1}m^{-1}$ or Fm^{-1})
ε_r	Dielectric constant or relative permittivity
τ	Relaxation time (s)
σ	Conductivity ($\Omega^{-1}m^{-1}$)

1. INTRODUCTION

This chapter will briefly introduce the fundamentals and applications of field effect transistors (FETs) and explain the difference between silicon and amorphous silicon. The objectives of the research are also introduced in this chapter. The motivation for the research came from previous experimental results that are briefly discussed.

1.1 Field Effect Transistors

A transistor is an electronic device used to control the flow of electricity; an example, of concern to this thesis, is the field effect transistor. A FET has four terminals that are known as source, gate, drain and substrate. In the field effect transistor, the channel defines the current path in the semiconductor. A gate voltage generates an electric field that controls the channel region to block or allow the flow of carriers from the source to the drain. The FET acts like a resistor, where the resistance is controlled by the gate voltage. This is why FETs are sometimes called voltage controlled resistors. The following paragraph introduces the various types of FETs and explains how they operate.

FETs can be classified into two main groups: insulated gate field effect transistors (IGFETs) and junction field effect transistors (JFETs). In an IGFET, an insulator prevents conduction between the gate and the channel. IGFETs can be made from bulk semiconductor such as a silicon wafer or a thin layer of semiconductor; the latter are sometimes referred to as thin-film transistors (TFTs). The most common structure for an IGFET is the metal-oxide semiconductor FET (MOSFET). MOSFETs and TFTs are the most important and commonly used semiconductor devices today. JFETs use a reverse biased p-n junction to separate the gate from the channel. JFETs are not part of my research and will not be discussed further.

MOSFETs come in four varieties depending on the channel doping (n-type or p-type) and the mode of operation (enhancement-mode (Figure 1(a)) or depletion-mode (Figure 1(b))).

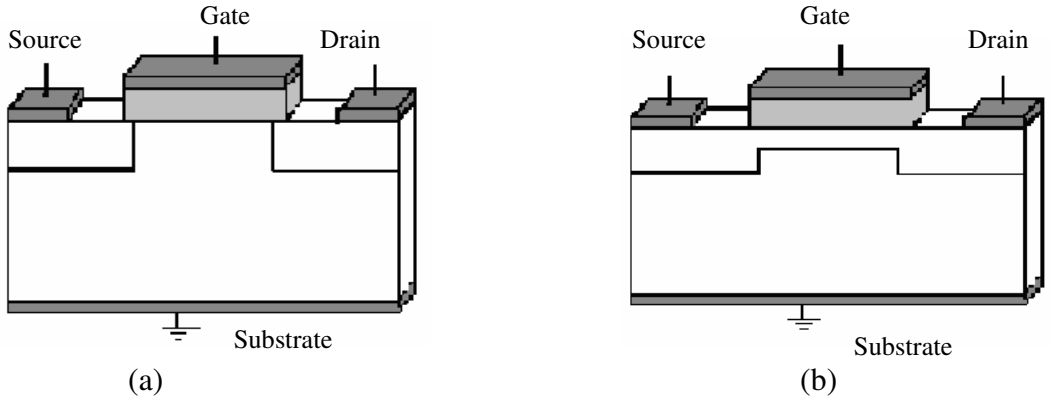

Figure 1 Basic structures of enhancement-mode and depletion-mode FET.

In all varieties of FETs, the transistor behavior is due to the field effect. That is, a voltage applied to the gate will attract one sign of carrier and repel the other sign of carrier from the region just under the insulator and thus alter the densities of carriers. The channel region of a FET is shown in Figure 2. In depletion-mode devices, the number of carriers in the channel is reduced by the field effect leading to an increase in resistance with the gate voltage, whereas in an enhancement-mode device the number of carriers is increased, and the resistance is decreased with the gate voltage.

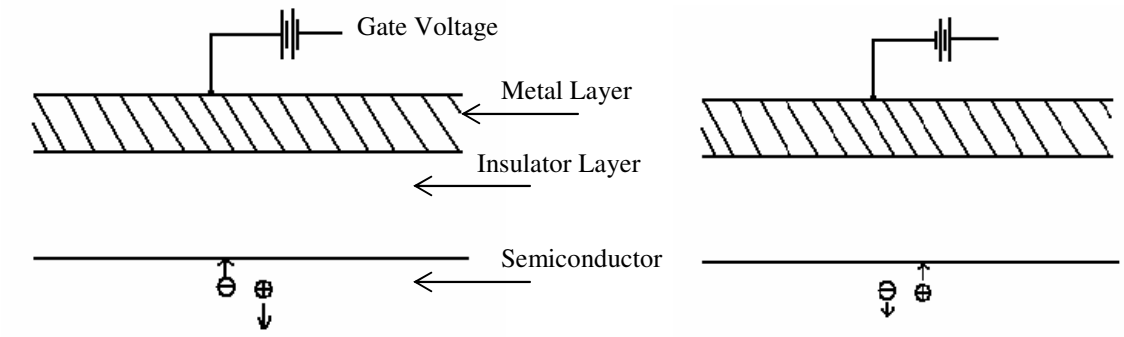

Figure 2 A voltage applies to the gate.

The operation in the actual devices is more complicated because the junction with the drain and the source is also important. Also, the shape and size of the conducting channel in the FET vary when different gate voltages are applied. Let us consider the operation of a p-type substrate enhancement-mode MOSFET (Figure 3). The source and the drain are doped n^+. A

negative gate voltage will attract holes to the semiconductor insulator interface. By increasing the negative gate voltage, more holes will be attracted and a p^+ region at the interface will form (Figure 3(a)). However, the n^+ p^+ interfaces at the source and drain prevent any significant current from flowing through the channel because no matter what voltage is applied from source to drain one of the n^+ p^+ junctions will be reverse-based. On the other hand, a positive gate voltage will attract electrons, and electrons recombine with holes leading to a region depleted of carriers (Figure 3(b)). No current flows between the source and drain. As the gate voltage (V_g) is increased, the size of depletion region increases until a threshold voltage (V_{th}) is reached where electrons start to accumulate. Above the threshold voltage $(V_g > V_{th})$, an n-type channel forms (Figure 3(c)). The junction between the channel and either source or drain is n n^+ which is ohmic, and current can now flow when a source-drain voltage (V_{ds}) is applied. If $V_{ds} = 0\text{V}$, then the thickness of the channel is uniform along its length. For $V_{ds} > 0\text{V}$, the potential along the channel increases from zero at the source to V_{ds} at the drain. Because the voltage drop from gate to drain is less than the voltage drop from gate to source, the field effect is less at the drain causing the channel to narrow across the device. If the gate voltage and the drain voltage satisfy the conditions $V_g > V_{th}$ and $V_{ds} \geq V_g - V_{th}$, then "pinch off" occurs, that is, the channel depth goes to zero before reaching the drain. Under the "pinch off" condition, there is not enough potential difference between the gate and channel to maintain the inversion region near the drain. The depletion region will close the channel (Figure 3(d)). As the potential at the drain is increased further, the "pinch off" point moves toward the source (Figure 3(e)).

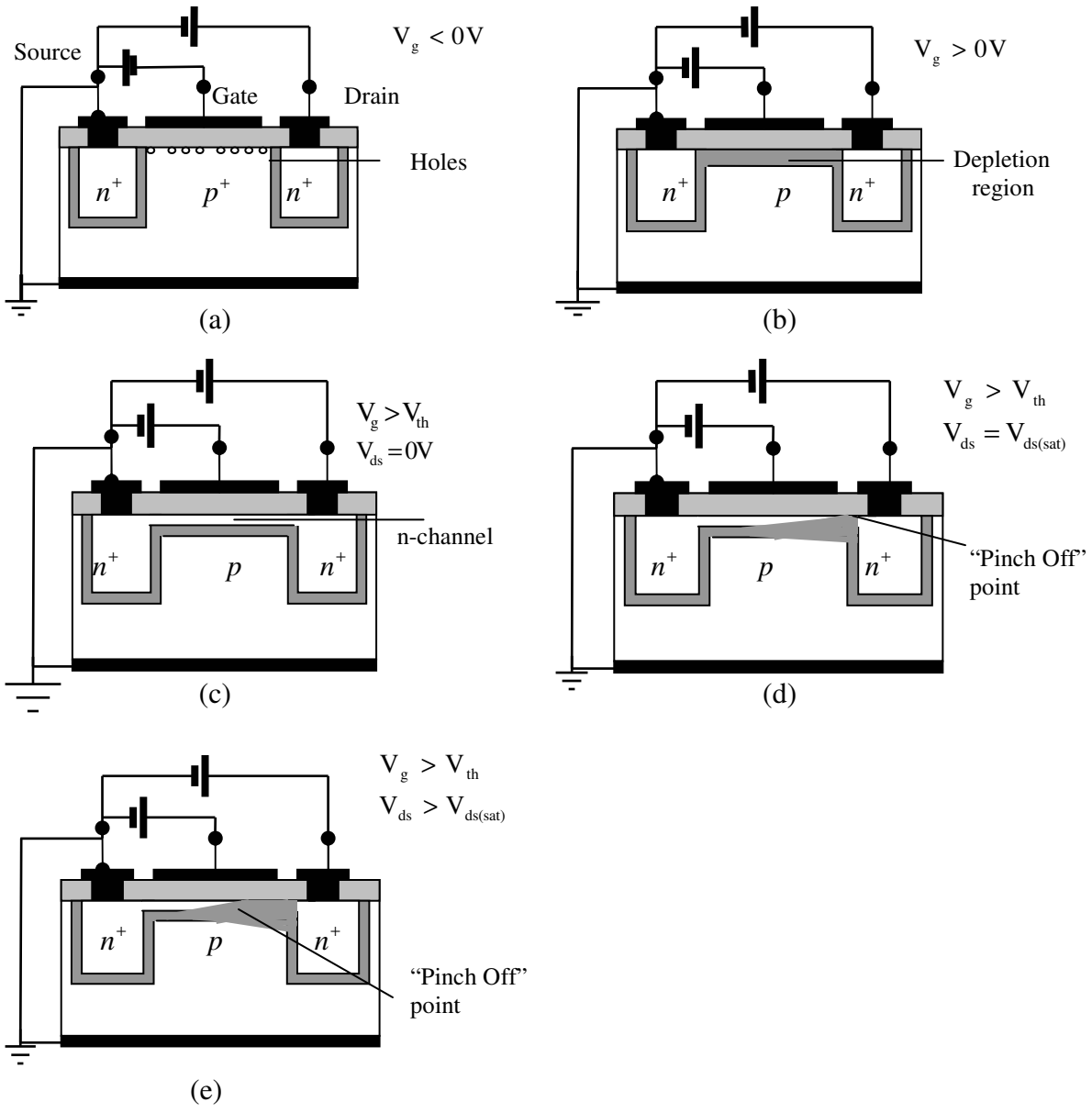

Figure 3 Operation of a p-type enhancement-mode FET [1].

However, current continues to flow because there is a potential drop between the source and the "pinch off" point that results in a current flow in the part of the channel that remains inverted. The carriers that reach the "pinch off" point are injected into the depleted region and continue to the drain.

1.2 Applications of TFTs

TFTs are commonly used in large area microelectronics. Active matrix liquid crystal displays use a TFT to control each pixel line. Sensor arrays also use TFTs to gate the detector signals. Of interest to researchers at the University of Saskatchewan are the two dimensional TFT arrays used in digital x-ray imagers. A flat panel x-ray detector uses a photoconductor combined with an active matrix array (AMA). Figure 4 shows how a flat panel detector signal chain is used in medical diagnostics. There are two types of detectors depending on how the x-rays are detected: indirect conversion or direct conversion. In indirect conversion, the x-rays are converted into visible light by a scintillation layer and then the visible light is detected by the photoconductor. In direct conversion, the photoconductor is sensitive to x-rays that directly produce electron-hole pairs.

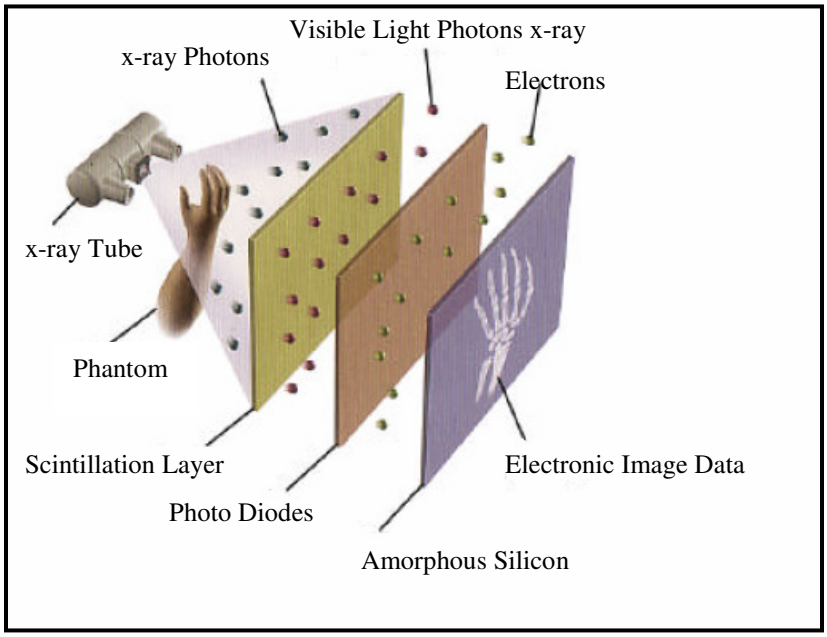

Figure 4 The flat panel detector signal chain (indirect conversion) [2].

In both cases a signal is produced for each pixel that is gated by the TFT array. The structure of an active matrix array and the cross section of a direct conversion detector are shown in Figure 5. In indirect conversion, the visible light is converted to a current in a photodiode that is gated by the TFT to a sense amplifier. In direct conversion, the absorbed x-rays produce electron-hole pairs that are separated in the photoconductor (e.g. stabilized a-Se) by an applied electric field

(Figure 5(a)). The charge is collected on a capacitor that is periodically discharged through the TFT into an integrating amplifier. The total amount of charge is proportional to the x-ray flux hitting the pixel.

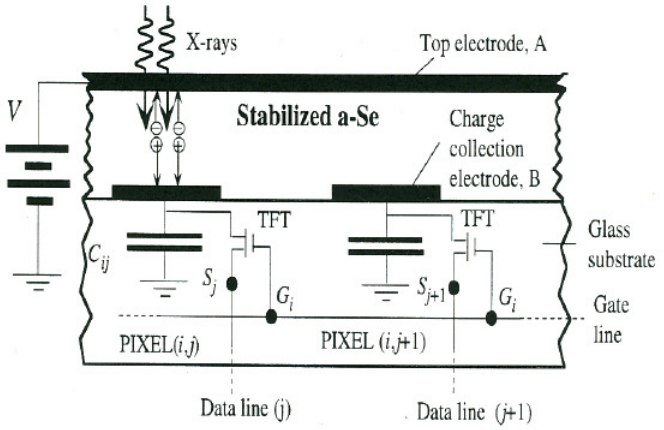

(a)

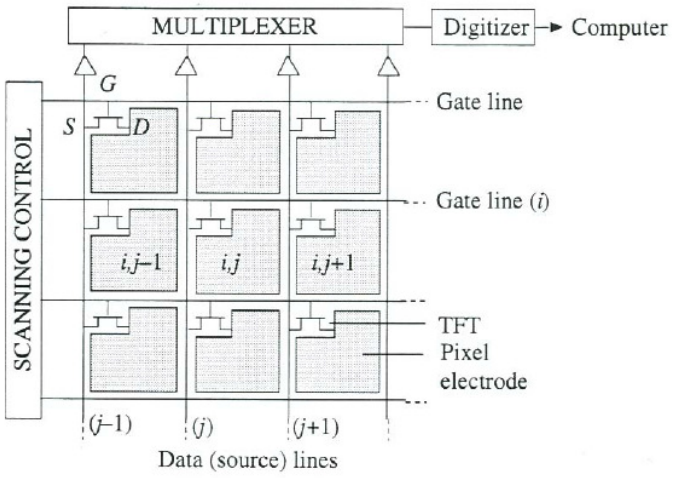

(b)

Figure 5 (a) Cross section of two pixels in a direct conversion x-ray detector [3].
(b) Schematic diagram of an active matrix array [3].

The detector is composed of an active matrix array that has $m \times n$ TFT based individual pixels. Figure 5(b) shows that all the TFTs in a row have their gates connected and all the TFTs in a column are connected to an amplifier. When a gate line i is activated, all the TFTs in that

row are turned on. The charges stored in the pixel capacitances are read out row by row and transferred to a computer until all the matrix arrays are read out.

The performance of the detector is limited by the overall signal to noise ratio. The noise can come from many sources including shot noise in the x-ray flux, gate-line resistance and data-line resistance generated Johnson noise, current generated shot noise, and pixel noise. The pixel noise can come from charge trapped in the TFT, the current channel of the TFT, and the photodiode or photoconductor. The TFTs contribute to the overall noise of the detector, and for this reason it is necessary to understand the origins of the TFT noise.

1.3 Silicon and Amorphous Silicon

Silicon is a chemical element with valence four, and each atom is normally bonded to four neighboring silicon atoms. Solid silicon can form a continuous crystalline lattice, as shown in Figure 6(a) [4]. Crystalline silicon is used to manufacture integrated circuits and is also the most widely used photovoltaic material.

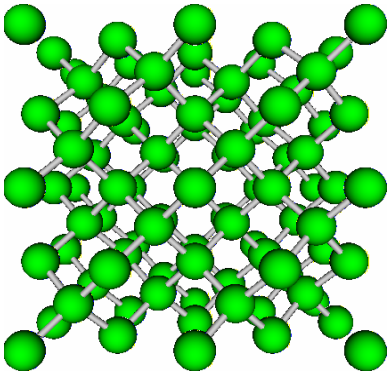

(a) Silicon structure [4]

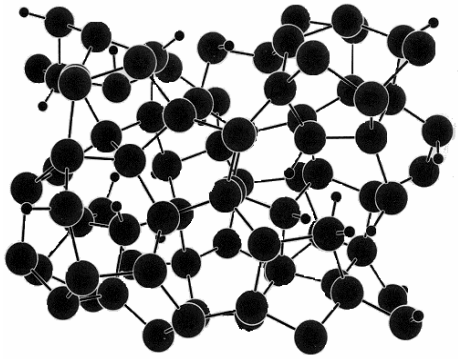

(b) Amorphous silicon structure [5]

Figure 6 Basic structures of silicon and amorphous silicon.

Amorphous silicon is the non-crystalline form of silicon. The atoms lack the regular ordered structure of a crystal. Some atoms may have fewer than four nearest neighbors in which case a bond is unsatisfied, this bond is known as dangling bond. In amorphous silicon although

almost every atom is still bonded to four others, the network of atoms is disordered, as schematically shown in Figure 6(b) [5]. Therefore, disorder of the atomic structure is the main feature that distinguishes amorphous from crystalline semiconductors. Because the covalent bonds between the atoms in amorphous silicon are similar to those in crystalline silicon, and most atoms have the same number of neighbors, and similar average bond lengths and bond angles, the two materials have roughly similar overall electronic structure. However, the high concentration of dangling bonds in amorphous silicon prevents it from being used in electronic devices since the material can not be doped and has no field effect. In 1969, Chittick et al. made the first hydrogenated amorphous silicon (a-Si:H). Adding hydrogen passivates the dangling bonds greatly lowering their density. Ten years later, Le Comber et al. made the first a-Si:H thin film transistor [6]. Since then a-Si:H has been widely used in many applications, such as the active layer in thin-film transistors.

Compared to crystalline silicon, a-Si:H requires a low deposition temperature, and it can be deposited over a large area. Therefore, a-Si:H is much cheaper than crystalline silicon for applications requiring a thin-film semiconductor over a large area such as TFT arrays or photovoltaics. The electronic properties of amorphous silicon will be explained in more detail in chapter three.

1.4 Previous Work on a-Si:H TFTs

Mr. Kim was a master student under the supervision of Dr. Johanson. He did the physical measurements of the noise of a-Si:H TFTs. His research studied the characteristics of low frequency noise in a-Si:H TFTs and how the noise depends on gate voltage and source-drain current. Some results are shown in Figure 7 to Figure 9. He showed the magnitude of the noise was inversely proportional to gate voltage (Figure 7) and it was also inversely proportional to the channel length (Figure 8). He also found that the drain-source voltage had an effect on the noise, as shown in Figure 9 [7].

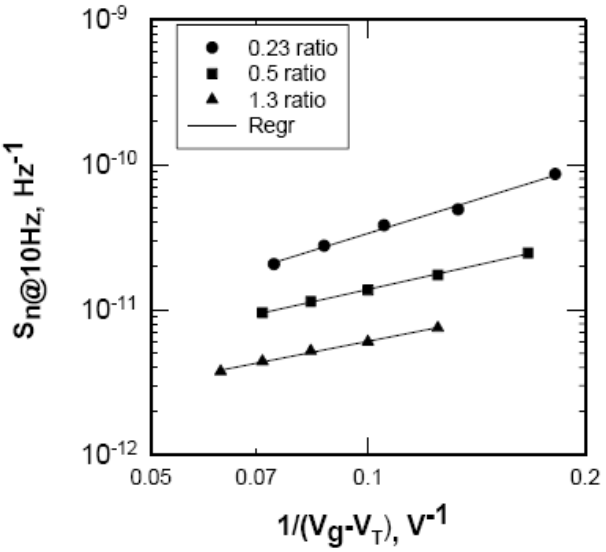

Figure 7 Normalized noise power density versus inverse gate voltage minus threshold voltage for different channel length TFTs [7].

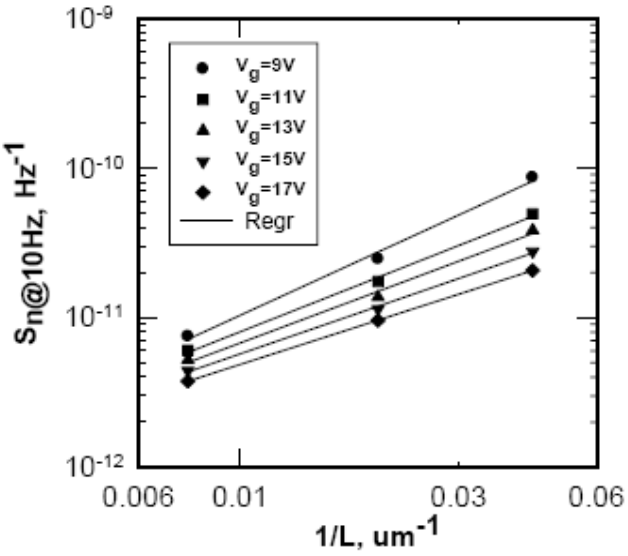

Figure 8 Normalized noise power density versus inverse channel length for different gate voltages V_g [7].

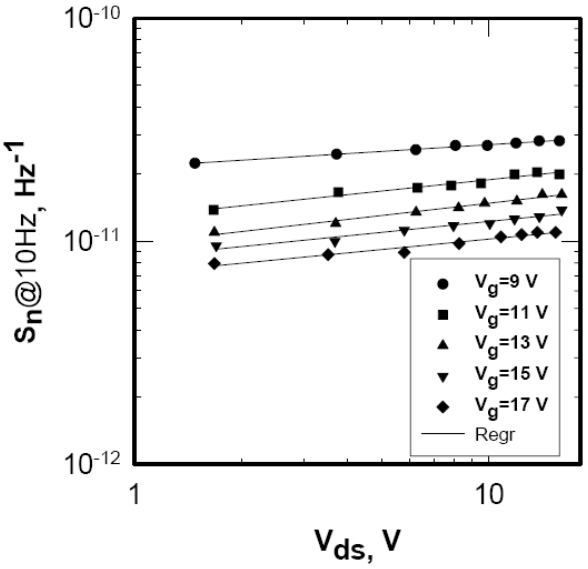

Figure 9 Normalized noise power density vs V_{ds} at different V_g for the 0.5 aspect ratio TFT [7].

1.5 Research Objectives

a-Si:H TFTs are commonly used as the switching devices in the detectors. The noise inherent in the a-Si:H TFTs contributes to the overall noise figure of the detectors and degrades the signal to noise ratio. Therefore, the noise is an important factor in the design of the devices. The noise of the TFTs must be measured and studied in order to reduce the noise level and as a consequence improve detector quality.

The primary goal of this research is to understand the measured noise of a-Si:H TFTs and in particular to test hypothesis put forward by Mr. Kim to explain the observed dependence on gate voltage, length and source-drain voltage. The goal is accomplished by simulating the operation of the a-Si:H TFT using the basic equations of electromagnetism and the known properties of a-Si:H. The results of the simulations allow a noise figure to be calculated and compared to the experimental results.

1.6 Thesis Outline

This thesis has been divided into six chapters. Chapter one briefly introduces field effect transistors, crystalline silicon, amorphous silicon and applications of a-Si:H TFTs. It also introduces the experimental results from previous experiments. Chapter two introduces the types of noise and the mathematics of noise analysis. Chapter three introduces the basic properties of amorphous silicon hydride. Chapter four explains the simulation in detail. Chapter five contains the simulation results. Chapter six presents conclusion and summary of suggestions for future work.

2. NOISE

Noise is any unwanted signal that reduces or distorts the quality of the signal and information carried by the signal. Intrinsic noise sources and extrinsic noise sources are two fundamental types of noise sources that affect electrical circuits. Intrinsic noise is generated by the components of an electrical circuit and depends on the particular device. Extrinsic noise is generated by the surrounding environment and interactions between circuits. Thermal noise, shot noise, flicker or $1/f$ noise and diffusion noise are the most commonly encountered types of intrinsic noise. These intrinsic noise sources produce random fluctuations. This chapter introduces the three most important intrinsic noise sources: thermal noise, shot noise and $1/f$ noise. Thermal noise and shot noise exist in all devices and produce "white noise"; that is the noise power density is the same at all frequencies. $1/f$ noise depends on frequency having a higher power density at lower frequencies. Thermal noise or shot noise are well understood, so I will briefly describe them. $1/f$ noise will be discussed in more detail. The last part of this chapter describes the mathematics used to describe or calculate any noise process.

2.1 Thermal Noise

Thermal noise, often referred to as Johnson noise, is generated by the random motion of charge carriers in electronic components. Inside of a conductor, carriers are in random motion because of thermal energy. The random motion causes a temporary net accumulation of charge on one side or the other side, leading to a fluctuating voltage across the material. However, there is no permanent accumulation of carriers so the mean value of the fluctuation is zero, but the root mean square (rms) value is not zero. Any device with a finite resistance produces thermal noise. The rms voltage is a function of the temperature and the resistance and is given by

$$V_{rms} = \sqrt{4kTRB} \tag{2.1}$$

where k is Boltzmann's constant (1.38×10^{-23}J/°K), T is the temperature expressed in Kelvin, R is the resistance, and B is the bandwidth of the equipment used to measure this noise [8]. A formula for the rms current can derive from Equation 2.1 and is given by

$$I_{rms} = \sqrt{\frac{4kTB}{R}} \tag{2.2}$$

The magnitude of thermal noise increases as the random motion increases with temperature. Equation 2.1 shows that thermal noise only disappears at absolute zero; however, there are three ways to reduce thermal voltage noise: narrow the bandwidth B, reduce resistance R or reduce the temperature T of electronic components. The thermal noise power spectral density can also be derived from Equation 2.1 and is given by

$$P = \frac{V^2}{R} = 4kTB$$

$$\frac{dP}{df} = 4kT \tag{2.3}$$

where f is the frequency. Equation 2.3 shows that thermal noise is white noise because power spectral density has equal power in each frequency interval df.

2.2 Shot Noise

Shot noise is a type of noise associated with the flow of discrete particles that are uncorrelated. For example: rain drops pattering on a roof, or photons of light hitting a detector. Another example is electric current flow because electrons and holes carry a discrete amount of charge. If the charge carriers are uncorrelated then the current will have shot noise. However, interactions between charge carriers can introduce correlations effectively suppressing randomly occurring bunches. Measured shot noise in a current is often less than predicted by theory, such as in the current flowing through a large resistor. But shot noise can be restored if the carriers

are randomized, for example, at a barrier such as a reversed bias *pn* junction (Figure 10). The current flow is determined by the carriers that get over the barrier – a random process. In order to observe shot noise, each carrier that enters the "observation" point or region must do so as a random event and independent of any other carrier that crosses this "observation" point.

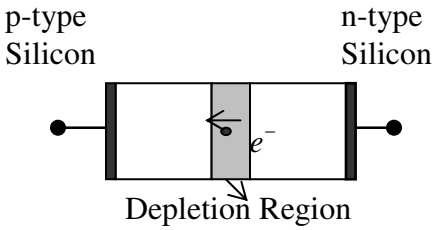

Figure 10 *pn* junction.

It is impossible to predict the motion of an electron, but it is possible to calculate the average net velocity of an electron or the average number of electrons drifting past a particular point or an "observation" region per time interval. The spectral density of shot noise can be deduced based on these assumptions.

2.2.1 Derivation of Shot Noise

Under forward bias in a *pn* junction, a carrier crossing the depletion region ("observation" region) of the junction is a random event and independent of the other carriers crossing this region, which is a Poisson process. The resulting current consists of a large number of independent current pulses. The average of these current pulses is a DC current. If we use an ideal ammeter (input impedance is zero) to measure the current then the ammeter shows that the current also has fluctuations [9].

The current flow can be described as a delta function. t_j are the random arrival times of the carriers. Then

$$I(t) = \sum_j q\delta(t - t_j) \tag{2.4}$$

N is defined as the number of carriers crossing the observation region in a time interval $[-\frac{T}{2},\frac{T}{2}]$. I_{DC} is the DC current. Then

$$I_{DC} = \frac{N}{T} q \tag{2.5}$$

The autocorrelation function of the current pulse is given by [10]

$$R_I(t') = \lim_{T\to\infty} \frac{1}{T} \int_{-T/2}^{T/2} I(t) I(t+t') dt \tag{2.6}$$

We apply Equation 2.4 to Equation 2.6 to find the autocorrelation of the delta function current pulse [9].

$$\begin{aligned} R_I(t') &= \lim_{T\to\infty} \frac{1}{T} \int_{-T/2}^{T/2} \sum_j q\delta(t-t_j) \sum_{j'} q\delta(t+t'-t_{j'}) dt \\ &= \lim_{T\to\infty} \frac{q^2}{T} \sum_j \sum_{j'} \int_{-T/2}^{T/2} \delta(t-t_j)\delta(t+t'-t_{j'}) dt \\ &= \lim_{T\to\infty} \frac{q^2}{T} \sum_j \sum_{j'} \delta(t_j - t_{j'} + t') \end{aligned} \tag{2.7}$$

The arrival times are equal $j = j'$, and the random arrival times of the carriers are equal $t_j = t_{j'}$. If there are N values of carriers t_j, Equation 2.7 changes to

$$R_I(t') = \frac{q^2}{T} N\delta(t') \tag{2.8}$$

Now, we apply Equation 2.5 to Equation 2.8, then

$$R_I(t') = qI_{DC}\delta(t') \tag{2.9}$$

The Wiener-Khintchine theorem states that the noise spectrum is the Fourier transform of the autocorrelation function, then

$$S_I(f) = 2\int_{-\infty}^{\infty} R_I(t')e^{-j2\pi ft'}dt' \tag{2.10}$$

where $S_I(f)$ is the power spectral density. We apply Equation 2.9 to Equation 2.10, then

$$S_I(f) = 2qI_{DC} \tag{2.11}$$

Equation 2.11 shows that the spectral density of shot noise is only a function of the DC current flowing through the device. Compared to thermal noise, shot noise can not be eliminated by lowering the temperature. The shot noise spectral density does not have any frequency dependence, i.e. white noise.

2.3 $1/f$ **or Flicker Noise**

$1/f$ noise arises from fluctuations in the resistance of a device, and $1/f$ noise dominates at low frequencies. When a constant voltage is applied across a resistor then the current fluctuates. Alternatively, if a constant current flows then the voltage across the resistor fluctuates. The excess noise has power spectral density proportional to $1/|f|^{\alpha}$, where α is usually in the range between 0.8 and 1.4 [11]. When α equals to 1, one has classic $1/f$ noise. $1/f$ noise exists in all electronic materials and devices. Unlike thermal or shot noise that is well understood, scientists still don't know where $1/f$ noise comes from for most materials or any systematic way to reduce $1/f$ noise. There is no general theory to describe $1/f$ noise.

2.3.1 Scale Invariance

Classic $1/f$ noise can be characterized by a power spectral density function,

$$\overline{S_x(\omega)} = c/|\omega| \tag{2.12}$$

where c is a constant value that is independent of frequency ω [11]. The integrated power in the spectrum between the angular frequencies ω_1 and ω_2 is given by

$$P_x(\omega_1, \omega_2) = \frac{1}{2\pi}\int_{\omega_1}^{\omega_2} \overline{S_x(\omega)}d\omega = (c/2\pi)\ln(\omega_2/\omega_1) \tag{2.13}$$

Equation 2.13 shows that the integrated power is a constant value when there is a fixed frequency ratio ω_2/ω_1. For example, the total noise power between $1\,\text{Hz}$ and $100\,\text{Hz}$ is the same as that between $10\,\text{Hz}$ and $1000\,\text{Hz}$. This property of $1/f$ noise is known as scale invariance and such noise is sometimes called "pink noise" [11]. However, the integrated power P_x goes to infinite as either ω_1 goes to zero or ω_2 goes to infinity. This property is unphysical since it implies an infinite energy. But the divergence is logarithmic which is very slow and at some low ω_1 and high ω_2 the spectrum likely changes so that the integrated power remains finite.

2.3.2 Hooge's Empirical Relation

There are two major theories to analyze and explain $1/f$ noise in the FETs: Hooge's empirical relation and McWhorter's theory. In general, a fluctuation in resistance occur either because the mobility changes or the number density of carriers changes. Hooge's empirical relation for $1/f$ noise through his study of mobility fluctuations in metals. He characterized the noise using the formula

$$\frac{\overline{S_r(\omega)}}{R_0^2} = \frac{\alpha_H}{N_{total}|f|} \tag{2.14}$$

where N_{total} is the total number of charge carriers in the sample, R_0 is the mean resistance, $\overline{S_r(\omega)}$ is the power spectral density of the resistance fluctuations, and constant $\alpha_H \approx 2\times10^{-3}$ [11]. The Hooge's empirical relation describes $1/f$ noise relates to the number of the charge carriers; therefore, $1/f$ noise could occur from fluctuations in the generation-recombination or trapping of the charge carriers.

Equation 2.14 was proposed by Hooge in 1969. The original claim for the Equation 2.14 applies to all homogeneous materials that have been modified to include only those cases where lattice scattering is much larger than impurity scattering and where boundary scattering is negligible [11]. If impurity scattering is significant, then α_H in the Equation 2.14 needs to be reduced by a factor

$$\left(\frac{\mu_{imp}}{\mu_{lat} + \mu_{imp}}\right)^2$$

where μ_{imp} is the mobility associated with impurity, μ_{lat} is the mobility associated with lattice scattering [11]. The Hooge's empirical relation is not a general formula and failed in several experiments, such as α_H is 2×10^3 times larger than Hooge's α_H in the Equation 2.14 when Dutta et al measured $1/f$ noise in copper whiskers silver [11].

2.4 Mathematical Analysis of Noise

The most important feature of noise is randomness; the value of the measured quantity noise is unpredictable, and it is impossible to write a general equation for the value as function of time. However, noise can be described using a statistical description.

Without loss of generality, let the mean value be zero. Then the variance is equal to the mean square value. Consider an observed noise process $n(t)$ for the time interval $[0,T]$. Then the time average $\overline{n(t)}$ is defined as

$$\overline{n(t)} = \lim_{T\to\infty} \frac{1}{T} \int_0^T n(t)dt \tag{2.15}$$

The rms value of the noise process is defined as

$$n_{rms} = \sqrt{\overline{n^2(t)}} = \sqrt{\frac{1}{T} \int_0^T n^2(t)dt} \tag{2.16}$$

If two noise sources $n_1(t)$ and $n_2(t)$ are added $(n_1(t) + n_2(t))$, then the total average noise power is given by

$$\begin{aligned} \overline{n_{total}^2(t)} &= \overline{[n_1(t) + n_2(t)]^2} \\ &= \overline{n_1^2} + \overline{2n_1(t)n_2(t)} + \overline{n_2^2(t)} \\ &= \overline{n_1^2(t)} + 2\gamma\sqrt{\overline{n_1^2(t)}}\sqrt{\overline{n_2^2(t)}} + \overline{n_2^2(t)} \end{aligned} \tag{2.17}$$

where γ is the correlation coefficient between the $n_1(t)$ and $n_2(t)$. If $\gamma = 0$, there is no correlation and equation 2.17 can be written as

$$\overline{n_{total}^2(t)} = \overline{n_1^2(t)} + \overline{n_2^2(t)} \tag{2.18}$$

2.4.1 Energy Theorems

Noise power spectral density describes how the noise power of a signal varies with frequency. The derivation of the noise power spectral density begins with the Fourier transform of a signal $x(t)$

$$X(j\omega) = \int_{-\infty}^{\infty} x(t) \exp(-j\omega t) dt \tag{2.19}$$

where $x(t)$ can be real or complex, but for an actual signal $x(t)$ will be real [11]. When $x(t)$ is a real function of time, the Fourier transform shows conjugate symmetry:

$$X(j\omega) = X^*(-j\omega) \tag{2.20}$$

where the asterisk (*) designates complex conjugation [11]. The inverse of the integral transform in Equation 2.19 is given by

$$x(t) = (1/2\pi) \int_{-\infty}^{\infty} X(j\omega) \exp(j\omega t) d\omega \tag{2.21}$$

Assume the noise process is observed over the time interval $[0, T]$. $x_1(t)$ and $x_2(t)$ are two time functions and their Fourier transforms are $X_1(j\omega)$ and $X_2(j\omega)$. Then

$$\int_{-\infty}^{\infty} x_1(t) x_2^*(t) dt = (1/2\pi) \int_{-\infty}^{\infty} X_1(j\omega) X_2^*(j\omega) d\omega \tag{2.22}$$

Let

$$\begin{aligned} x_1(t) &= x_T(t+\tau) \\ x_2(t) &= x_T(t) \end{aligned} \tag{2.23}$$

where x_T is the gated process and τ is a delay time. Equation 2.22 is replaced by Equation 2.19, 2.20, 2.21, and 2.23, then

$$\int_{-\infty}^{\infty} x_T(t+\tau) x_T(t) dt = (1/2\pi) \int_{-\infty}^{\infty} |X_T(j\omega)|^2 \exp(j\omega\tau) d\omega \tag{2.24}$$

where $x_T(t)$ is a real process, so $x^*(t) = x(t)$ [11]. When $\tau = 0$, Equation 2.24 reduces to

$$\int_{-\infty}^{\infty}[x_T(t)]^2 dt = 1/2\pi \int_{-\infty}^{\infty} |\, X_T(j\omega)\,|^2 \; d\omega \tag{2.25}$$

which is called Plancherel's theorem or the energy theorem [11]. Each side of Equation 2.25 equals to the total energy, therefore, power is proportional to $[x_T(t)]^2$, and the time integral is proportional to the total energy in the process which is always finite for $T < \infty$. Thus $\left|X_T(j\omega)\right|^2$ can be interpreted as the energy density of the process in the frequency domain and has the units of $energy/Hertz$. The average power in the gated noise process is the total energy divided by T. The power remains finite as T goes to infinity for any physical process, so the average power for a non-gated process is given by

$$\lim_{T\to\infty}\frac{1}{T}\int_{-\infty}^{\infty}[x_T(t)]^2 dt = \lim_{T\to\infty}(1/2\pi)\int_{0}^{\infty}\frac{2\,|\,X_T(j\omega)\,|^2}{T}\,d\omega \tag{2.26}$$

Therefore, the power spectral density of the stationary process $x_T(t)$ is defined as

$$\overline{S_x(\omega)} = \lim_{T\to\infty}\frac{2\overline{\left|X_T(j\omega)\right|}^2}{T} \tag{2.27}$$

Equation 2.27 shows that the power spectral density is related to the square of the Fourier transform of the signal. However in an experiment, instead of measuring the signal for an infinite time, the signal is measured for a finite amount of time. But if T is long enough so that sufficient averaging is done then the resulting power spectrum should closely approximate the theoretical spectrum of Equation 2.27.

3. a-Si:H TFTs DEVICE CHARACTERISTICS

This chapter introduces the basic physical properties of amorphous silicon and thin film transistors (TFTs) made from a-Si:H. The first section describes the general structural and electronic features of amorphous solids. Next, the important subject of the density of states (DOS) for a-Si:H is discussed. Trapping into localized states influences the operation of the TFTs and is explored in detail. The last part of the chapter describes several TFT structures and explains the operational principles for the thin film transistor.

3.1 The Basic Properties of Amorphous Silicon

In chapter one, the basic differences between amorphous and crystalline materials were briefly described; amorphous materials are disordered, have broken bonds and do not have long range crystal symmetry but amorphous materials have the same amount of bonding as in crystalline materials, as shown in Figure 6. The following sections describe the properties of amorphous silicon.

3.1.1 Atomic Structure

Amorphous silicon is not completely disordered. The covalent bonds between the silicon atoms in amorphous silicon are similar to crystalline silicon. Most atoms have the same number of neighbors, the same average bond lengths and bond angles in amorphous and crystalline silicon.

The structural disorder is characterized by deviations in the bond lengths and bond angles. Three principal features of the structure of an amorphous material are the short range order, the long range disorder and the coordination defects. The short range order only concerns the nearest neighbor of a given atom and the bonds are most strongly influenced by the neighboring atom, which is almost the same in amorphous and crystalline silicon. Unlike crystalline silicon, amorphous silicon has no long range order. The farther from a given atom, the less able one can

predict the positions of other atoms. The coordination defects occur where an atom has too many or too few bonds.

Potential fluctuations due to structural disorder cause changes to the electronic states. The effect of this type of disorder on the electronic states is to localize those states near the band edges and causes strong scattering of the charge carriers. Structural defects like broken bonds also create localized electronic states. The correspondence between features of the atomic structure and the resulting electronic properties is shown in Table 3.1 [12]. The bonding disorder determines most of the electronic properties of an amorphous material by influencing the density of states function.

Structure	Electronic Properties
Bonding disorder	Band tails, Localization, Scattering
Structural defects	Deep strongly localized electronic states in the band gap

Table 3.1 The correspondence between features of the atomic structure and the resulting electronic properties [12].

3.1.2 Density of States

In a given energy band, there are many energy levels but they are not distributed uniformly in energy. The density of states (DOS) is defined as the number density of electronic states per unit energy interval. The density of states is very important since it determines the electrical transport, recombination, trapping and doping etc. Structural disorder alters the electronic density of states from that of a crystal. The most significant difference between the crystalline and amorphous states comes at the band edges. For ideal crystalline silicon, there are no states in energy gap between the conduction and valence bands. But for amorphous silicon, the band edges of a crystal are replaced by a broadened tail of states extending into the energy gap, which originates from the deviations of the bond length and bond angle arising from the structural disorder. Therefore, for amorphous silicon, electronic states that are localized are

found in the former energy gap. Figure 11(a) shows the density of states in a crystalline material. Figure 11(b) shows that extended states continue to exist in the bands but connect smoothly into the localized states in the amorphous material.

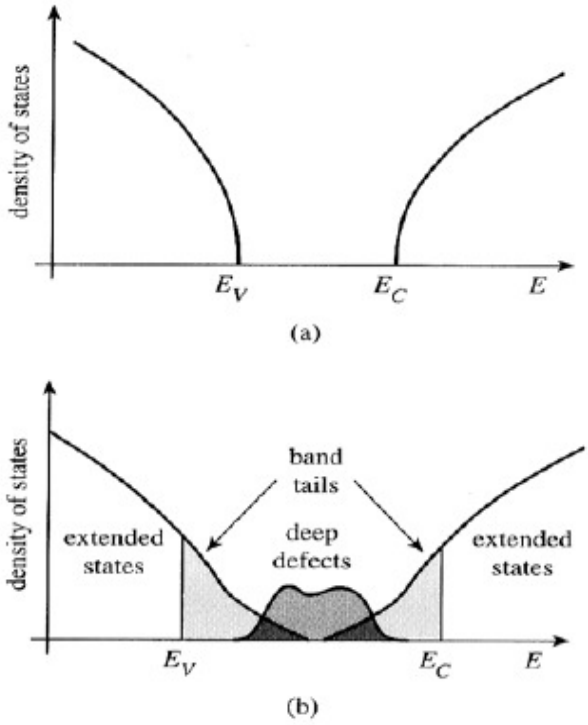

Figure 11 (a) The density of states in a crystalline material [13].
(b) The density of states in an amorphous material [13].

Figure 11(b) clearly shows that energy can be divided into different energy ranges that contain extended states and localized states. The localized states are separated from the extended states by the mobility edge. The extended states are in the energy ranges below the mobility edge of the valance band (E_v) and above the mobility edge of the conduction band (E_c). The extended states allow the electrons or holes to move and have a finite mobility value. The localized states are the energy ranges between the mobility edge of the valence band and the mobility edge of the conduction band. The mobility value for the localized states is essentially zero. The localized states consist of two types: band-tail states and deep-gap (deep-defect) states. The band-tail states are near the mobility edges and extend into the mobility gap from both conduction and valence band edges. The band-tail states control electronic transport at the mobility edge due to

the electrons or holes being trapped into the band-tails for a certain time resulting in a decrease in their effective mobility. The width of the band-tail depends on the degree of bond angle and length disorder [12]. The deep defect states are caused by dangling bonds in the amorphous material. Dangling bonds occur when an atom is missing a neighbor. The neutral dangling bond has a single unpaired electron. If the electron is lost to the atom, the result is a positively charged defect that can trap electrons. Alternatively, an additional electron can be added resulting in a negatively charged stated that can trap holes. Deep defects control electronic properties through electrons or holes trapping and de-trapping from the defects and recombination through the defects.

3.1.3 Trapping

Trapping occurs when mobile electrons or holes are captured by localized states in the mobility gap. Trapping can be classified into two types; one type of trapping leads to recombination and the other type of trapping is temporary. For example, an electron is captured by a localized state. Later a hole is captured into the same state and effectively the electron has gone from the conduction band to the valence band and has recombined with the hole. Therefore, the electron is removed from the conduction band due to the recombination with the hole. Figure 12(a) illustrates an electron recombination [1]; similar arguments can apply to a hole recombination. However, an electron captured by a localized state can after a period of time gain energy from lattice vibrations and be excited back into the conduction band. The electron is then available for conduction again. A deeper trap requires longer times on average before the electron is released. The trap release time is given by $t_r = v_o^{-1} \exp(\Delta E / kT)$, where v_o is the trap release frequency and ΔE is the trap depth. The deep states are more likely to act as recombination centers and band-tail states act as temporarily traps. Figure 12(b) illustrates an electron trapping and de-trapping, similar arguments can be applied to hole traps [1].

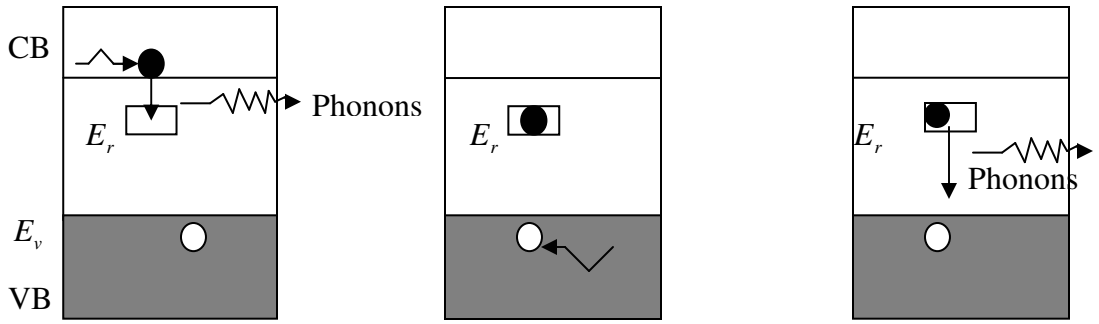

Figure 12 (a) Recombination [1]. An electron in the conduction band (CB) is trapped by a localized state at energy E_r. Later, a hole in the valence band (VB) is trapped by the same state, resulting in recombination.

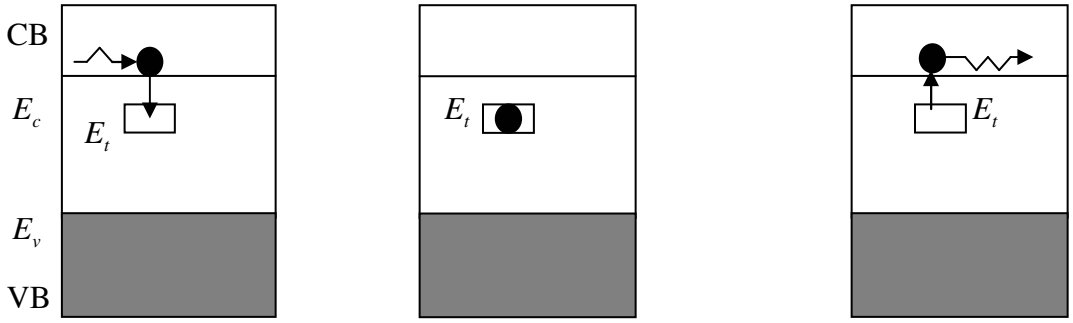

Figure 12 (b) Trapping and de-trapping of electrons [1]. An electron in the conduction band (CB) is trapped by a localized states at energy E_t. Later, the electron is thermally excited back to the conduction band.

3.1.4 Noise Generation via Trapping

Noise can arise due to carriers trapping and de-trapping in localized states or recombination of carriers. The localized states can either be the band-tail or defect states in the amorphous silicon or interface states or states in an adjacent material. The band-tail states act as temporarily traps, which trap and release mobile electrons. There is no current while trapped electrons do not move. The current fluctuates down as electrons trap and fluctuates up as electrons release which is called trap-release noise. Recombination of carriers also generates fluctuation noise in the current but this is much smaller than trap-release noise. $1/f$ noise in a crystalline or amorphous silicon field effect transistor arises from the thermal excitation of electrons from interface states to the conduction band.

3.2 Hydrogenated Amorphous Silicon Thin Film Transistor (TFT) Structure

A thin film transistor (TFT) (Figure 13) is either a depletion-mode transistor or an accumulation-mode transistor. However, a depletion-mode transistor is difficult to achieve using a-Si:H due to a high defect density of doped material, which makes it difficult to deplete the channel. A p-channel accumulation-mode TFT is also not used since the mobility of holes is much lower than electrons, which gives the p-channel accumulation-mode transistor a lower current by about a factor of 100 in amorphous silicon [12]. An n-channel accumulation-mode transistor is a widely used structure and consists of the a-Si:H channel, the gate dielectric, the source, the drain, and the gate contacts.

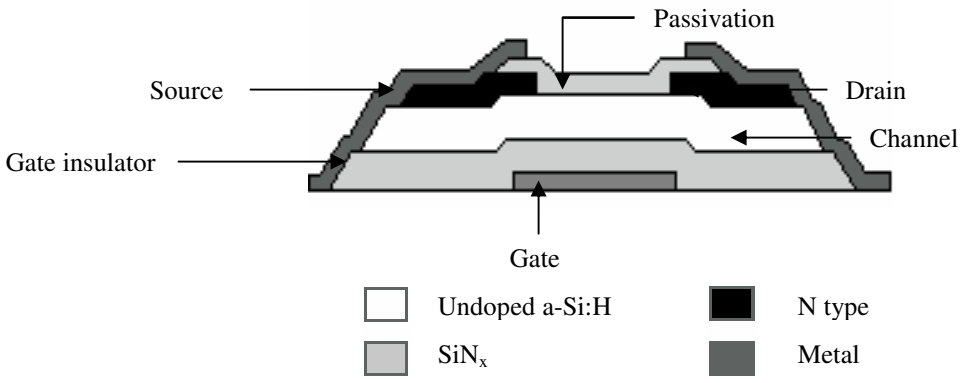

Figure 13 An inverted-staggered (bottom-gate) a-Si:H TFT structure [12].

A number of TFT structures are used in different applications depending on greater density and lower cost advantages. The physical structure of some popular TFT structures are discussed. Figure 14 describes a number of the most popular TFT structures according to the position of the active layer, the gate, the gate insulator, the semiconductor and the contacts. A staggered TFT has the gate and the contact electrodes on opposite sides of the semiconductor, whereas a coplanar TFT has the gate and the contact electrodes on the same side of the semiconductor. Both structures come in two versions; one with the gate above the semiconductor and an inverted configuration with the gate below. Figure 14(a) and 14(b) show the staggered TFT structures that have the semiconductor layer between the insulator and the electrodes where as the coplanar TFT structures have the electrodes in or between gate insulator and semiconductor, as shown in Figure 14(c) and 14(d).

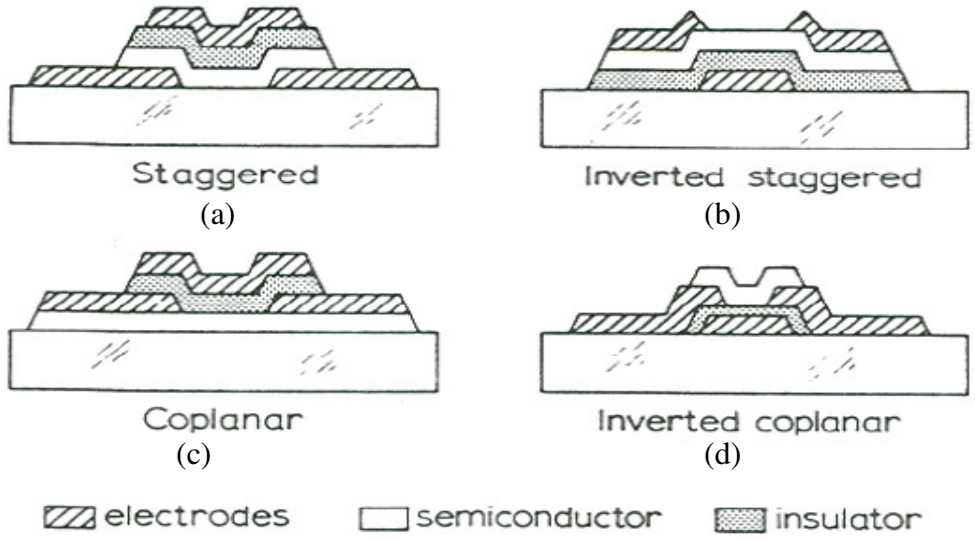

Figure 14 A few of the most popular a-Si:H TFT structures [14].

The inverted-staggered (bottom-gate) a-Si:H TFT structure is the most widely used in the manufacture of TFT arrays. Inverted-staggered a-Si:H comes in two versions: the back-channel-etched (BCE) structure and the etch-stopper (ES) structure, as shown in Figure 15(a) and 15(b).

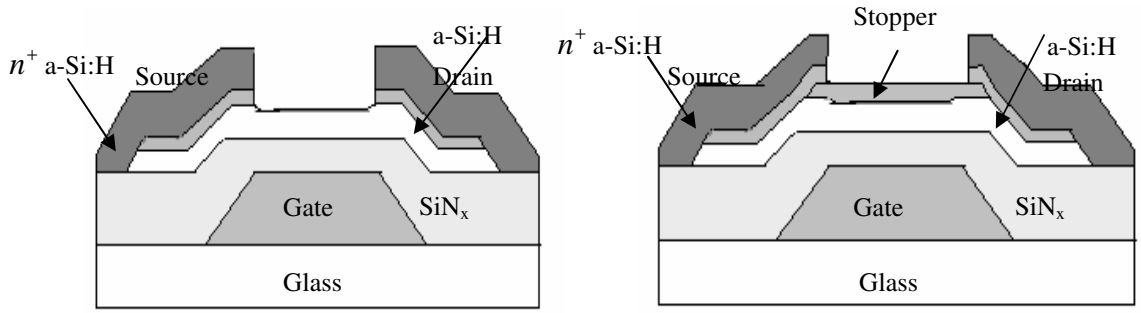

(a) (b)

Figure 15 (a) Cross sectional view of a back-channel-etched (BCE) a-Si:H TFT [14].
(b) Cross sectional view of an etch-stopper (ES) a-Si:H TFT [14].

Fabrication of an inverted-staggered a-Si:H TFT (Figure 14(b)) starts with the formation of the gate on the substrate and then the gate insulator. a-Si:H and source or drain layers are deposited sequentially. Compared to the ES TFT (Figure 15(b)), the BCE TFT (Figure 15(a)) requires fewer fabrication steps; however, the BCE TFT needs a rather thick intrinsic layer to have enough process margin for n^+ etching. The n^+ layer between the source and drain electrodes need to be over etched to completely remove the n^+ a-Si:H layer over the channel [14]. In an ES a-Si:H TFT, another SiN_x layer coves on the top of the back-channel, so the n^+ etch process is easy and the intrinsic layer can be very thin [14]. However, the processing is more complicated than the BCE a-Si:H TFT, since the ES a-Si:H TFT requires more process steps to fabricate. The ES a-Si:H TFT has a little higher extrinsic mobility and much lower photo-leakage current than the BCE a-Si:H TFT due to a very thin intrinsic layer. The extrinsic field effect mobility is reduced by increasing the intrinsic layer thickness because of the series contact resistance between n^+ and channel [14]. Thus, the series contact resistance can be lower in the ES a-Si:H TFT because of the thin intrinsic layer. Similarly, the photo-leakage current of a-Si:H TFT is increased by the thickness of the intrinsic layer, which admits less optical absorption of light from the backlight [14]. Therefore, many LCD companies are more likely to use the BCE a-Si:H TFT due to this reason.

3.2.1 Operation of TFT

The inverted-staggered a-Si:H TFT operates in the accumulation mode. Accumulation occurs when a voltage applied to the gate increases the majority carriers beyond the equilibrium value in the semiconductor. Energy band diagrams are used to explain how the energy changes when there are different applied gate voltages. Figure 16 shows the band bending profiles and the occupancy of the electronic states for different gate voltages.

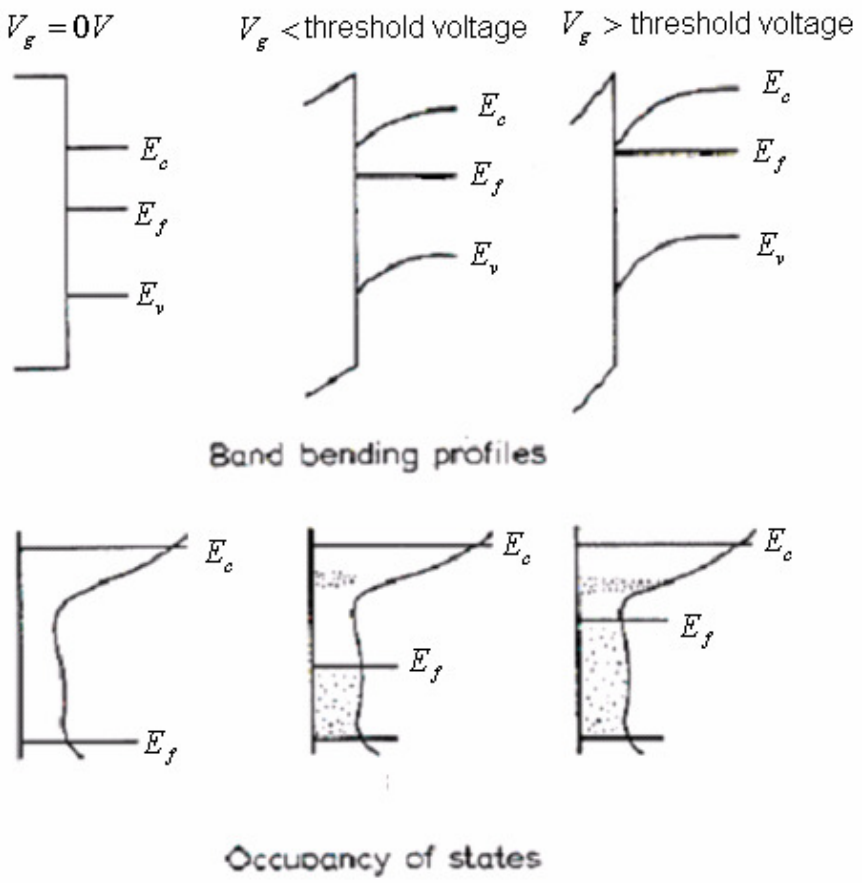

Figure 16 The basic operation of the a-Si:H TFTs [15].

If no gate voltage (V_g) is applied, the energy bands do not bend, the energy bands stay at the flat band conditions and the Fermi level (E_f) is close to mid-gap. No electrons accumulate near the interface and no electrons are injected. If a positive gate voltage is applied, the energy bands bend down and the Fermi level moves up. Electrons accumulate near the interface to form a conduction channel. Then if a positive drain voltage is applied, the drain-source current flows from the drain to the source and increases linearly with drain voltage ($V_{ds} << V_g$) in the linear region and is almost constant with increasing drain voltage in the saturated region. Many of the electrons that are injected into the channel region are trapped into deep localized states. The trapping process continues until all deep states lower than the new Fermi level are full and equilibrium is established. When a large positive gate voltage is applied, the energy bands bend

downward more than before, the Fermi level moves up but still below the tail states. The injected carrier density exceeds that in the deep states.

4 SIMULATION: METHODS AND APPLICATIONS

4.1 Fundamental Equations

In order to calculate the noise of the a-Si:H based on a simulation of operation of the TFTs, an a-Si:H TFT is simulated by numerically by solving the fundamental transport equations for various gate and drain-source voltages. Three main fundamental transport equations must be considered: Poisson's equation, the current equation and the continuity equation. These equations are solved numerically with the appropriate boundary conditions in order to obtain the charge density profile in the TFT. The following section describes the fundamental equations in detail.

4.1.1 Poisson's Equation

Poisson's equation relates the electric potential V to the charge density ρ. It can be deduced from one of the Maxwell's equations (Gauss' law for electricity),

$$\vec{\nabla} \cdot \vec{D} = \rho \tag{4.1}$$

which contains the electrical behavior of the material,

$$\vec{D} = \varepsilon \vec{E} = \varepsilon_0 \varepsilon_r \vec{E} \tag{4.2}$$

where $\vec{D}$ is the displacement field, $\vec{E}$ is the electric field, ε is the permittivity of a medium, ε_r is the dielectric constant or relative permittivity and ε_0 is the permittivity of free space $(8.8542 \times 10^{-12}\ \mathrm{CV^{-1}m^{-1}}$ or $\mathrm{Fm^{-1}})$. The electric field is derived from the electric potential.

$$\vec{E} = -\vec{\nabla} \vec{V} \tag{4.3}$$

Poisson's equation (Equation 4.4) is deduced from Equation 4.1, 4.2 and 4.3.

$$\vec{\nabla}\cdot\vec{D}=\rho=\vec{\nabla}\cdot\varepsilon\vec{E}=\varepsilon\cdot(\vec{\nabla}\cdot\vec{E})+\vec{E}\cdot(\vec{\nabla}\varepsilon)$$

$$=-\varepsilon(\vec{\nabla}\cdot\vec{\nabla}V)+\vec{E}\cdot(\vec{\nabla}\varepsilon)$$

$$\nabla^2V=\vec{\nabla}\cdot(\vec{\nabla}V)=-\frac{\rho}{\varepsilon}+\frac{\vec{E}\cdot(\vec{\nabla}\varepsilon)}{\varepsilon} \tag{4.4}$$

where the charge density ρ in a semiconductor is determined by the concentration of electrons and holes (with concentrations n and p, respectively), and ionized acceptors and ionized donors (with concentrations N_A^- and N_D^+, respectively).

$$\rho=(p-n-N_A^-+N_D^+)q \tag{4.5}$$

Thus, Poisson's equation 4.4 changes to

$$\nabla^2V=-\frac{(p-n-N_A^-+N_D^+)q}{\varepsilon}+\frac{\vec{E}\cdot(\vec{\nabla}\varepsilon)}{\varepsilon} \tag{4.6}$$

The second term of Poisson's equation ($\frac{\vec{E}\cdot(\vec{\nabla}\varepsilon)}{\varepsilon}$) is zero if the permittivity (ε) is a constant value.

4.1.2 Current Equation

The current equation describes how the charge carriers move through the conductor. The motion of the charge carriers involves drift and diffusion. Thus, the current equations are also known as the drift-diffusion equations. The drift current density is caused by the electric field, $\vec{E}$, acting on mobile carriers. The diffusion current density is caused by the charge carriers moving randomly from a higher concentration to a lower concentration. The electron current density due to drift is

$$\vec{J}_{e-drift}=qn_f\mu_e\vec{E} \tag{4.7}$$

where n_f is the concentration of the mobile electrons, μ_e is the mobility of electrons, q is the magnitude of the electron charge (1.602×10^{-19} C). The electron current density due to the electron diffusion is

$$\vec{J}_{e-diffusion} = qD_e\vec{\nabla}n_f \tag{4.8}$$

where D_e is the electron diffusion coefficient, which is related to the mobility by Einstein's relation.

$$D_e = \mu_e\frac{kT}{q} \tag{4.9}$$

Thus, the total electron current density is obtained by adding the drift and the diffusion current density.

$$\begin{aligned}\vec{J}_e &= \vec{J}_{e-drift} + \vec{J}_{e-diffusion} \\ &= qn_f\mu_e\vec{E} + qD_e\vec{\nabla}n_f\end{aligned} \tag{4.10}$$

Similarly, the total current density due to the hole drift and the hole diffusion is

$$\vec{J}_h = qp_f\mu_h\vec{E} - qD_h\vec{\nabla}p_f \tag{4.11}$$

where p_f is the concentration of the mobile holes, the hole diffusion coefficient is $D_h = \mu_h\frac{kT}{q}$ and μ_h is the mobility of holes.

4.1.3 Continuity Equation

The continuity equation describes the change in carrier density over time due to the difference between the flux of leaving and entering carriers (Figure 17).

$$\vec{\nabla} \cdot \vec{J} = -\frac{\partial \rho}{\partial t} \tag{4.12}$$

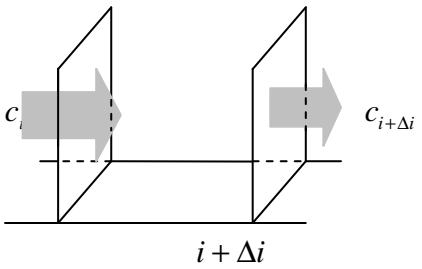

Figure 17 Leaving and entering flux of charge carriers in a region.

The current equals the sum of the electron current and the hole current then the continuity equations for electrons and holes are

$$\vec{J} = \vec{J}_e + \vec{J}_h \tag{4.13}$$

Since ionized donors and acceptors are fixed, the change in charge density in a region is due to the change in n and p

$$\frac{\partial \rho}{\partial t} = -q\frac{\partial n}{\partial t} + q\frac{\partial p}{\partial t} \tag{4.14}$$

So the continuity equation becomes

$$\vec{\nabla} \cdot \vec{J} = \vec{\nabla} \cdot (\vec{J}_e + \vec{J}_h) = -\frac{\partial(-qn + qp)}{\partial t} \tag{4.15}$$

However, charge carrier density can also change due to generation and recombination. If the electron (hole) generation rate is G_e (G_h) and recombination rate is R_e (R_h) then we expect $G_e = G_h$ and $R_e = R_h$, Equation 4.15 becomes

$$\vec{\nabla} \cdot \vec{J}_e + \vec{\nabla} \cdot \vec{J}_h = \frac{\partial(qn)}{\partial t} - \frac{\partial(qp)}{\partial t} + G_e(-q) - R_e(-q) + G_h(q) - R_h(q) \tag{4.16}$$

The continuity equation can now be separated into one for electrons and one for holes

$$\vec{\nabla} \cdot \vec{J}_e = \frac{\partial(qn)}{\partial t} + G_e(-q) - R_e(-q)$$

$$\vec{\nabla} \cdot \vec{J}_e = q(\frac{\partial n}{\partial t} - G_e + R_e)$$

$$\vec{\nabla} \cdot \vec{J}_h = -q(\frac{\partial p}{\partial t} - G_h + R_h)$$

Solving for the change in carrier concentration gives

$$\frac{\partial n}{dt} = \frac{\vec{\nabla} \cdot \vec{J}_e}{q} - R_e + G_e \tag{4.17}$$

$$\frac{\partial p}{dt} = -\frac{\nabla \cdot \vec{J}_h}{q} - R_h + G_h \tag{4.18}$$

4.2 Discrete or Finite Difference Equations

I need to solve the differential equations in two dimensions for the geometry of the TFT in the plane that includes the channel. Since an analytical solution is very difficult in two dimensions, the solution will be obtained numerically. To solve the differential equations numerically, they must be converted to finite difference equations. The finite difference method or the discrete method is used to solve Poisson's equation, the current density equation and the continuity equation. I am interested in solving the FET in two dimensions so the finite

difference equations will be developed for two dimensional Cartesian coordinates x and y. The FET is most naturally simulated using a rectangular grid of points with spacing Δx and Δy in the x and y directions respectively. Let the grid point $(x_n, y_m) = (n\Delta x, m\Delta y)$, where $n = 1,2,...,N$, $m = 1,2,...,M$, as shown in Figure 18.

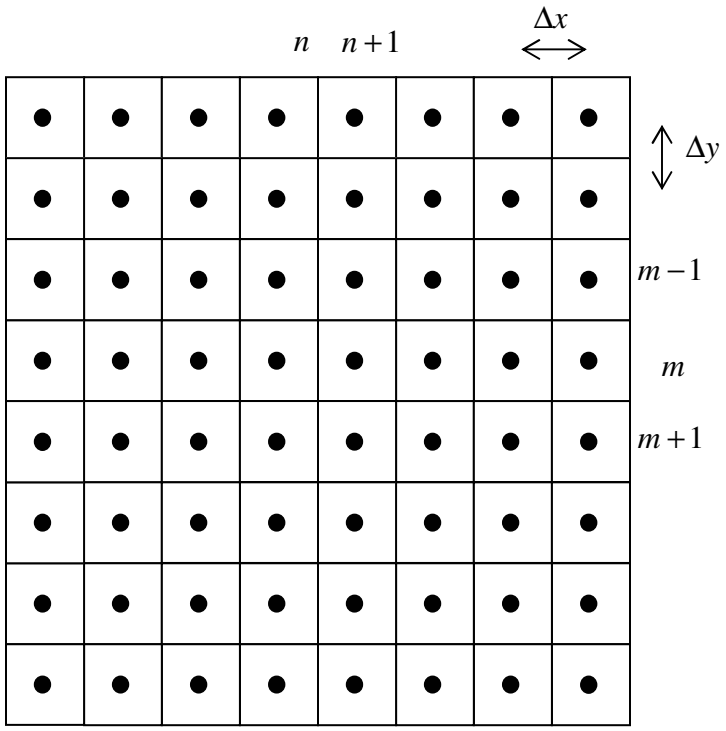

Figure 18 Grid points evenly spaced along the x and the y directions.

The simulations store quantities such as potential and electron density for each grid point. The continuous equations need to be rewritten for the discrete grid. A method to determine the appropriate finite difference equation for a continuous equation uses the Taylor series expansion for the quantities. Let f be a continuous quantity (such as potential) then

$$f(x) = f(x_0) + f'(x_0)(x - x_0) + \frac{f''(x_0)}{2!}(x - x_0)^2 + ... + \frac{f^{(n)}(x_0)}{n!}(x - x_0)^n + R_n(x) \qquad (4.19)$$

where $R_n(x)$ is a remainder term. Suppose the continuous equation involves a derivative of f, such as $\frac{\partial f}{\partial x}$. We need a finite difference formula to calculate $\frac{\partial f}{\partial x}$ at a point x_n. The Taylor series expansion for $f(x_{n+1})$ is to first order

$$f(x_{n+1}) \approx f(x_n) + f'(x_n)(x_{n+1} - x_n) \tag{4.20}$$

Solving for $f'(x_n)$ gives the required finite difference equation

$$f'(x_n) = \frac{\partial f(x_n)}{\partial x} = \frac{f(x_{n+1}) - f(x_n)}{x_{n+1} - x_n}$$

$$\frac{\partial f(x_n)}{\partial x} = \frac{f(x_{n+1}) - f(x_n)}{\Delta x} \tag{4.21}$$

A different equation can be derived using the Taylor series expansion for $f(x_{n-1})$,

$$f(x_{n-1}) = f(x_n) - f'(x_n)(x_n - x_{n-1}) \tag{4.22}$$

Subtracting Equation 4.20 and Equation 4.22 yield,

$$f(x_{n+1}) - f(x_{n-1}) = 2f'(x_n)\Delta x$$

So

$$f'(x) = \frac{f(x_{n+1}) - f(x_{n-1})}{2\Delta x} \tag{4.23}$$

The choice of the finite difference equation depends on the particular simulation.

The electric field is solved from the electric potential V (Equation 4.3). The electric field $\vec{E}$ points to right in $+x$ direction or points to upward in $+y$ direction are positive values, as shown in Figure 19.

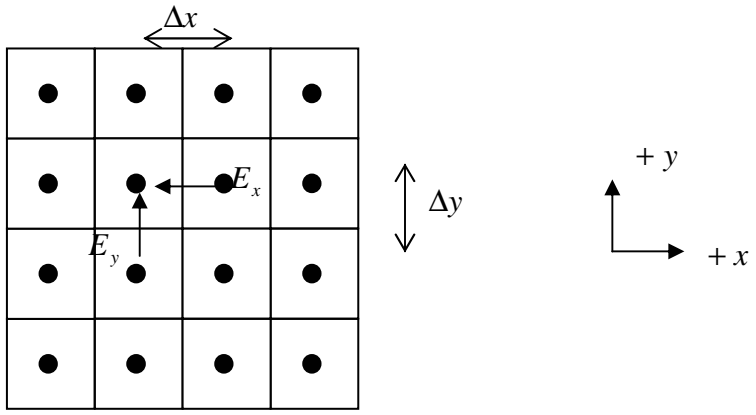

Figure 19 The electric field $\vec{E}$ in x and y direction.

The electric field equation can be derived using Equation 4.21,

$$\begin{aligned}\vec{E} &= -\vec{\nabla}V \\ &= -(\frac{\partial V}{\partial x}\hat{x} + \frac{\partial V}{\partial y}\hat{y}) \\ &= -(\frac{V_{n+1,m} - V_{n,m}}{\Delta x}\hat{x} + \frac{V_{n,m+1} - V_{n,m}}{\Delta y}\hat{y})\end{aligned} \tag{4.24}$$

Similarly, the electron current density equation (Equation 4.10) and the hole current density equation (Equation 4.11) can be calculated by using Equation 4.21.

$$\begin{aligned}\vec{J}_e &= qn_f\mu_e\vec{E} + qD_e\vec{\nabla}n_f \\ &= qn_f\mu_e(-(\frac{V_{n+1,m} - V_{n,m}}{\Delta x})\hat{x} - (\frac{V_{n,m+1} - V_{n,m}}{\Delta y})\hat{y}) + qD_e(\frac{n_{n+1,m} - n_{n,m}}{\Delta x}\hat{x} + \frac{n_{n,m+1} - n_{n,m}}{\Delta y}\hat{y})\end{aligned} \tag{4.25}$$

$$\vec{J}_h = qp_f \mu_h \vec{E} - qD_h \vec{\nabla} p_f$$

$$= qp_f \mu_h (-(\frac{V_{n+1,m} - V_{n,m}}{\Delta x})\hat{x} - (\frac{V_{n,m+1} - V_{n,m}}{\Delta y})\hat{y}) - qD_h (\frac{p_{n+1,m} - p_{n,m}}{\Delta x}\hat{x} + \frac{p_{n,m+1} - p_{n,m}}{\Delta y}\hat{y}) \quad (4.26)$$

Using Equation 4.21 to calculate the continuity equations (Equation 4.17 and Equation 4.18) and the continuity equations become

$$\frac{\partial n}{dt} = \frac{\nabla \cdot \vec{J}_e}{q} + G_e - R_e$$

$$= \frac{1}{q}(\frac{J_{n+1,m} - J_{n,m}}{\Delta x}\hat{x} + \frac{J_{n,m+1} - J_{n,m}}{\Delta y}\hat{y}) + G_e - R_e \quad (4.27)$$

$$\frac{\partial p}{dt} = -\frac{\nabla \cdot \vec{J}_h}{q} + G_h - R_h$$

$$= -\frac{1}{q}(\frac{J_{n+1,m} - J_{n,m}}{\Delta x}\hat{x} + \frac{J_{n,m+1} - J_{n,m}}{\Delta y}\hat{y}) + G_h - R_h \quad (4.28)$$

4.3 Two Dimensional Poisson's Solver

There are several methods which can be used to solve the Poisson's equation. At beginning, I was studying the simulation by the finite element method (FEM). However, FEM requires more analysis time to solve the Poisson's equation and for the simulation the computation time is an important factor. To reduce analysis time and improve the algorithm of the analysis code, a simple method for solving the Poisson's equation is the Gauss-Seidel method (GS) or Jacobi's method. The successive over-relaxation method (SOR) is based on the GS method, and the SOR method is used to solve the $2D$ Poisson's equation in order to speed up the simulation time. The SOR method is similar to the GS method, but the SOR method takes less analysis time, so the SOR method is used effectively. A detailed description of the Jacobi's method, the GS method and the SOR method are given in the following sections.

4.3.1 The Jacobi's Method

The Jacobi's method is the simplest iterative method to solve an equation $Ax = b$. The Jacobi's method is given current values $x^{(k)} = (x_1^{(k)}, x_2^{(k)}, x_3^{(k)}, ..., x_n^{(k)})$ to find new values $x^{(k+1)} = (x_1^{(k+1)}, x_2^{(k+1)}, x_3^{(k+1)}, ..., x_n^{(k+1)})$ [16], where k corresponds to the particular iteration. For example,

$$
\begin{aligned}
a_{11}x_1^{(k+1)} + a_{12}x_2^{(k)} + ... + a_{1n}x_n^{(k)} &= b_1 \\
a_{21}x_1^{(k)} + a_{22}x_2^{(k+1)} + ... + a_{2n}x_n^{(k)} &= b_2 \\
&\vdots \\
a_{n1}x_1^{(k)} + a_{n2}x_2^{(k)} + ... + a_{nn}x_n^{(k+1)} &= b_n
\end{aligned}
$$

These equations can be written as a matrix.

$$
\begin{bmatrix} a_{11} & 0 & \cdots & 0 \\ 0 & a_{22} & \ddots & \vdots \\ \vdots & \ddots & \ddots & 0 \\ 0 & \dots & 0 & a_{nn} \end{bmatrix} \begin{bmatrix} x_1^{(k+1)} \\ x_2^{(k+1)} \\ \vdots \\ x_n^{(k+1)} \end{bmatrix} + \begin{bmatrix} 0 & a_{12} & \cdots & a_{1n} \\ a_{21} & 0 & \ddots & \vdots \\ \vdots & \ddots & \ddots & a_{n-1n} \\ a_{n1} & \dots & a_{nn-1} & 0 \end{bmatrix} \begin{bmatrix} x_1^{(k)} \\ x_2^{(k)} \\ \vdots \\ x_n^{(k)} \end{bmatrix} = \begin{bmatrix} b_1 \\ b_2 \\ \vdots \\ b_n \end{bmatrix} \tag{4.29}
$$

Let $D = \begin{bmatrix} a_{11} & 0 & \cdots & 0 \\ 0 & a_{22} & \ddots & \vdots \\ \vdots & \ddots & \ddots & 0 \\ 0 & \dots & 0 & a_{nn} \end{bmatrix}$, $L = \begin{bmatrix} 0 & 0 & \cdots & 0 \\ a_{21} & 0 & \ddots & \vdots \\ \vdots & \ddots & \ddots & 0 \\ a_{n1} & \dots & a_{nn-1} & 0 \end{bmatrix}$ and $U = \begin{bmatrix} 0 & a_{12} & \cdots & a_{1n} \\ 0 & 0 & \ddots & \vdots \\ \vdots & \ddots & \ddots & a_{n-1n} \\ 0 & \dots & 0 & 0 \end{bmatrix}$,

Then, the matrix 4.29 changes to

$$
\begin{aligned}
Dx^{(k+1)} + (L+U)x^{(k)} &= b \\
x^{(k+1)} &= \frac{[(-L-U)x^{(k)} + b]}{D}
\end{aligned} \tag{4.30}
$$

Equation 4.30 can be solved based on the following condition [17]:

$$\frac{\left\| x^{(k)} - x^{(k-1)} \right\|}{\left\| x^{(k)} \right\|} < \delta$$

where δ is called relative approximate error. The iterations are stopped when the absolute relative approximate error is less than a pre-specified tolerance for all unknowns.
The Jacobi's method also can be written as

$$u_{m,n} = \frac{u_{m-1,n} + u_{m+1,n} + u_{m,n-1} + u_{m,n+1} + h^2 b_{m,n}}{4} \tag{4.31}$$

Equation 4.31 assumes mesh spaces along x and y directions are equal ($\Delta x = \Delta y = h$). Initial value can be any value. For example, we start with an initial value $u_{m,n,0} = 0$. To calculate the value for $u_{m,n,k+1}$ in terms of the previous iteration $u_{m,n,k}$, the following equation is used

$$u_{m,n,k+1} = \frac{u_{m-1,n,k} + u_{m+1,n,k} + u_{m,n-1,k} + u_{m,n+1,k} + h^2 b_{m,n,k}}{4} \tag{4.32}$$

where $u_{m,n,k}$ is an approximation for $u_{m,n}$ after the k th iteration. Equation 4.32 shows that $u_{m,n,k+1}$ is a linear combination of its four neighbor values $(u_{m-1,n,k}, u_{m+1,n,k}, u_{m,n-1,k}, u_{m,n+1,k})$, h and $b_{m,n,k}$. The iterations are stopped when the absolute relative approximate error is less than a pre-specified tolerance for all unknowns.

4.3.2 The Gauss-Seidel Method

The GS method is an improvement of the Jacobi's method. The GS method is given current values $x^{(k)} = (x_1^{(k)}, x_2^{(k)}, x_3^{(k)}, ..., x_n^{(k)})$ to find new values $x^{(k+1)}$ by solving equations

$$a_{11}x_1^{(k+1)} + a_{12}x_2^{(k)} + ... + a_{1n}x_n^{(k)} = b_1$$
$$a_{21}x_1^{(k+1)} + a_{22}x_2^{(k+1)} + ... + a_{2n}x_n^{(k)} = b_2$$
$$\vdots$$
$$a_{n1}x_1^{(k+1)} + a_{n2}x_2^{(k+1)} + ... + a_{nn}x_n^{(k+1)} = b_n$$

These equations also can be written as a matrix.

$$\begin{bmatrix} a_{11} & 0 & \cdots & 0 \\ a_{21} & a_{22} & \ddots & \vdots \\ \vdots & \ddots & \ddots & 0 \\ a_{n1} & \cdots & a_{nn-1} & a_{nn} \end{bmatrix} \begin{bmatrix} x_1^{(k+1)} \\ x_2^{(k+1)} \\ \vdots \\ x_n^{(k+1)} \end{bmatrix} + \begin{bmatrix} 0 & a_{12} & \cdots & a_{1n} \\ 0 & 0 & \ddots & \vdots \\ \vdots & \ddots & \ddots & a_{n-1n} \\ 0 & \cdots & 0 & 0 \end{bmatrix} \begin{bmatrix} x_1^{(k)} \\ x_2^{(k)} \\ \vdots \\ x_n^{(k)} \end{bmatrix} = \begin{bmatrix} b_1 \\ b_2 \\ \vdots \\ b_n \end{bmatrix} \tag{4.33}$$

$$(L + D)x^{(k+1)} + Ux^{(k)} = b$$
$$x^{(k+1)} = (L + D)^{-1}[-Ux^{(k)} + b]$$

The GS method works similar as the Jacobi's method except the GS method needs to track of the new variables $x^{(k+1)}$ and uses the new variables to calculate next equation. For example, if a value $u_{m,n}$ has been updated then $u_{m,n}$ is used immediately to calculate the new value of $u_{m,n,k+1}$. The GS iteration converges more rapidly than the Jacobi iteration because the GS iteration uses the latest updates to calculate new values. The following equation is used to calculate

$$u_{m,n,k+1} = \frac{u_{m-1,n,k+1} + u_{m+1,n,k} + u_{m,n-1,k+1} + u_{m,n+1,k} + h^2 b_{m,n,k}}{4} \tag{4.34}$$

where h is space between two points.

4.3.3 The Successive Over-Relaxation Method and Poisson's Equation

The successive over-relaxation method (SOR) is to improve the loop for the GS method by taking appropriate weight average of the $u_{m,n,k+1}$ and $u_{m,n,k}$. In this section, I will use Poisson's equation as an example to explain how the SOR method works. Poisson's equation (Equation 4.4) shows that

$$\vec{\nabla}^2 V = -\frac{\rho}{\varepsilon} + \frac{E(\vec{\nabla}\varepsilon)}{\varepsilon}$$

Poisson's equation can be reduced by the second order central difference operation that is defined at a grid point (m,n) and it can be written as

$$\frac{\partial^2 V_{m,n}}{\partial x^2} = \frac{V_{m+1,n} + V_{m-1,n} - 2V_{m,n}}{\Delta x^2} \tag{4.35}$$

$$\frac{\partial^2 V_{m,n}}{\partial y^2} = \frac{V_{m,n+1} + V_{m,n-1} - 2V_{m,n}}{\Delta y^2} \tag{4.36}$$

Then Poisson's equation is solved based on Equation 4.35 and Equation 4.36.

$$\frac{V_{m+1,n} + V_{m-1,n} - 2V_{m,n}}{\Delta x^2} + \frac{V_{m,n+1} + V_{m,n-1} - 2V_{m,n}}{\Delta y^2} = -\frac{\rho}{\varepsilon} + \frac{E(\vec{\nabla}\varepsilon)}{\varepsilon} \tag{4.37}$$

Now assuming permittivity (ε) is a constant value. Equation 4.37 changes to

$$\frac{V_{m+1,n} + V_{m-1,n} - 2V_{m,n}}{\Delta x^2} + \frac{V_{m,n+1} + V_{m,n-1} - 2V_{m,n}}{\Delta y^2} = -\frac{\rho}{\varepsilon} \tag{4.38}$$

There are two different conditions for mesh spaces along x and y directions: $\Delta x = \Delta y = h$ or $\Delta x \neq \Delta y$. Equation 4.38 changes to

If $\Delta x = \Delta y = h$, then Equation 4.38 becomes

$$V_{m+1,n} + V_{m-1,n} + V_{m,n-1} + V_{m,n+1} - 4V_{m,n} = -\frac{\rho}{\varepsilon} h^2 \tag{4.39}$$

If $\Delta x \neq \Delta y$, then Equation 4.38 becomes

$$\Delta y^2 (V_{m+1,n} + V_{m-1,n} - 2V_{m,n}) + \Delta x^2 (V_{m,n+1} + V_{m,n-1} - 2V_{m,n}) = -\frac{\rho}{\varepsilon} \Delta x^2 \Delta y^2$$

Then,

$$V_{m,n} = \frac{1}{2(\Delta x^2 + \Delta y^2)} (\Delta y^2 (V_{m-1,n} + V_{m+1,n}) + \Delta x^2 (V_{m,n+1} + V_{m,n-1}) + \frac{\rho}{\varepsilon} \Delta x^2 \Delta y^2) \tag{4.40}$$

We define residual R and let R equals to

$$R = \frac{1}{2(\Delta x^2 + \Delta y^2)} (\Delta y^2 (V_{m-1,n} + V_{m+1,n}) + \Delta x^2 (V_{m,n+1} + V_{m,n-1}) + \frac{\rho}{\varepsilon} \Delta x^2 \Delta y^2) - V_{m,n} \tag{4.41}$$

Thus, Equation 4.40 changes to

$$V_{m,n,k+1} = V_{m,n,k} + \omega R \tag{4.42}$$

where ω is called the over-relaxation parameter and defined as [18]

$$\omega_{(0)} = 1$$

$$\omega_{(\frac{1}{2})} = \frac{1}{(1 - \frac{\rho_{Jacobi}^2}{2})}$$

$$\omega_{(n+\frac{1}{2})} = \frac{1}{(1 - \frac{\rho_{Jacobi}^2 \omega_{(n)}}{4})}$$

where $n = \frac{1}{2}, 1, \frac{3}{2}, 2, ..., \infty$ and ρ is given by [18]

$$\rho_{Jacobi} = \frac{\cos\frac{\pi}{N_x} + (\frac{\Delta x}{\Delta y})^2 \cos\frac{\pi}{N_y}}{1 + (\frac{\Delta x}{\Delta y})^2} \tag{4.43}$$

The SOR method (Equation 4.42) is convergent if $0 < \omega < 2$. The SOR method is under-relaxation if $0 < \omega < 1$. If $\omega = 1$, then the SOR method changes to the GS method. If $1 < \omega < 2$, the SOR method is over-relaxation and gives faster convergence than the GS method under this condition [18].

Figure 20 shows grid points in red-black order and describes how the SOR method works. The SOR method starts at one corner and proceeds along the rows. However, instead of proceeding point one by one, the SOR method follows odd-even order or red-black order.

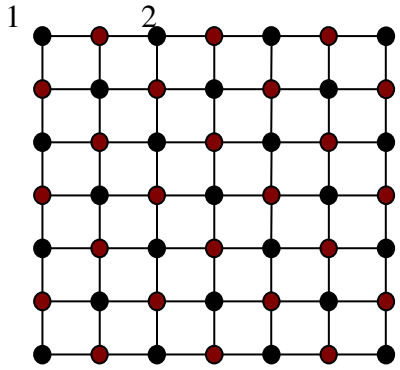

Figure 20 Grid points in red-black order.

For example, the SOR method starts at left top corner (point 1 from Figure 20) then calculates the third point (point 2) on the same row. During each iteration the black point is calculated by using the black point's neighbor points (red points). Similarly, the red points are evaluated using only the black points and vice versa. The iterations are stopped when the absolute relative approximate error is less than a pre-specified tolerance for all unknowns.

4.3.4 Verification of the Successive Over-Relaxation Method

It is helpful to have analytic solution for some specific cases and compare them with the numerical solution. So Poisson's equation is calculated to test the SOR method. I expand V and ρ in sine series consistent with the boundary conditions and they are defined as

$$V(x, y) = \sum_{m=1}^{\infty} a_m(y) \sin \frac{m\pi}{L_x} x \tag{4.44}$$

$$\rho(x, y) = \sum_{m=1}^{\infty} b_m(y) \sin \frac{m\pi}{L_x} x \tag{4.45}$$

V satisfies the boundary conditions $V(x, y) = 0$ for $x = 0$, $x = L_x$, $y = 0$ and $y = L_y$, as shown in Figure 21.

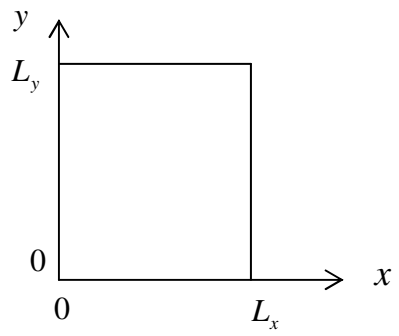

Figure 21 Boundary condition of y.

I insert Equation 4.44 and Equation 4.45 into Poisson's equation (Equation 4.4). Then Equation 4.38 changes to

$$-(\frac{m\pi}{L_x})^2 \sum_{m=1}^{\infty} a_m(y) \sin \frac{m\pi}{L_x} x + \sin \frac{m\pi}{L_x} x \sum_{m=1}^{\infty} \frac{\partial^2 a_m(y)}{\partial y^2} = -\frac{1}{\varepsilon} \sum_{m=1}^{\infty} b_m(y) \sin \frac{m\pi}{L_x} x \tag{4.46}$$

Simplify the Equation 4.46, it becomes

$$-(\frac{m\pi}{L_x})^2 a_m(y) + \frac{\partial^2 a_m(y)}{\partial y^2} = -\frac{b_m(y)}{\varepsilon} \tag{4.47}$$

where $b_m(y)$ is determined by inverting the sine series (Equation 4.45).

$$\begin{aligned}\int_0^{L_x} \rho \sin\frac{n\pi}{L_x} x dx &= \sum_{m=1}^{\infty} b_m(y) \sin\frac{m\pi}{L_x} \sin\frac{n\pi}{L_x} x dx \\ &= \sum_{m=1}^{\infty} b_m(y) \int_0^{L_x} \sin\frac{m\pi}{L_x} x \sin\frac{n\pi}{L_x} x dx \end{aligned} \tag{4.48}$$

Using the Fourier sine series definition [19], Equation 4.48 becomes

$$\begin{aligned}\int_0^{L_x} \rho \sin\frac{n\pi}{L_x} x dx &= \sum_{m=1}^{\infty} b_m(y) \frac{L_x}{2} \delta_{m,n} \\ &= \frac{L_x}{2} b_n \end{aligned} \tag{4.49}$$

Therefore $b_m(y)$ is deduced from Equation 4.49, and it gives

$$b_m(y) = \frac{2}{L_x} \int_0^{L_x} \rho(x, y) \sin\frac{m\pi}{L_x} x dx \tag{4.50}$$

We define $\rho(x, y) = \rho_0$ if $\frac{L_x - l_x}{2} < x < \frac{L_x + l_x}{2}$ and $\frac{L_y - l_y}{2} < y < \frac{L_y + l_y}{2}$; otherwise, $\rho(x, y) = 0$, as shown in Figure 22.

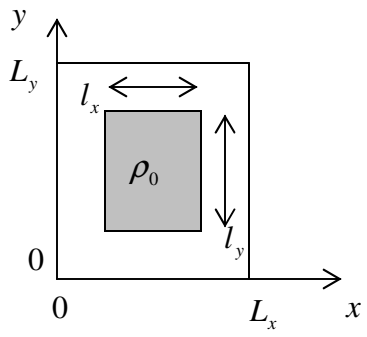

Figure 22 Distribution of charge density.

Let us put $\rho(x, y) = \rho_0$ at the condition $\frac{L_x - l_x}{2} < x < \frac{L_x + l_x}{2}$ into Equation 4.50, Equation 4.50 becomes

$$b_m = (-1)^{\frac{m-1}{2}} \frac{4\rho_0}{m\pi} \sin\frac{m\pi}{2}\frac{l_x}{L_x}, \quad m \text{ is an odd number.} \tag{4.51}$$

$$b_m = 0, \qquad m \text{ is an even number.} \tag{4.52}$$

Inserting Equations 4.51 and 4.52 into Equation 4.47, and solving a_m. Then V can be solved from Equation 4.44 if a_m is given.

$$V(x, y) = \sum_{m=1}^{\infty}\sum_{n=1}^{\infty} A_{m,n} \sin\frac{m\pi}{L_x} x \sin\frac{n\pi}{L_y} y \tag{4.53}$$

where $A_{m,n} = (-1)^{\frac{m-1}{2}} (-1)^{\frac{n-1}{2}} \frac{\rho_0}{\varepsilon} ((\frac{m\pi}{L_x})^2 + (\frac{n\pi}{L_y})^2)^{-1} \frac{16}{mn\pi^2} \sin(\frac{m\pi}{2}\frac{l_x}{L_x}) \sin(\frac{n\pi}{2}\frac{l_y}{L_y})$ for m is an odd number and n is an odd number. $A_{m,n} = 0$ for m is an even number and n is an even number.

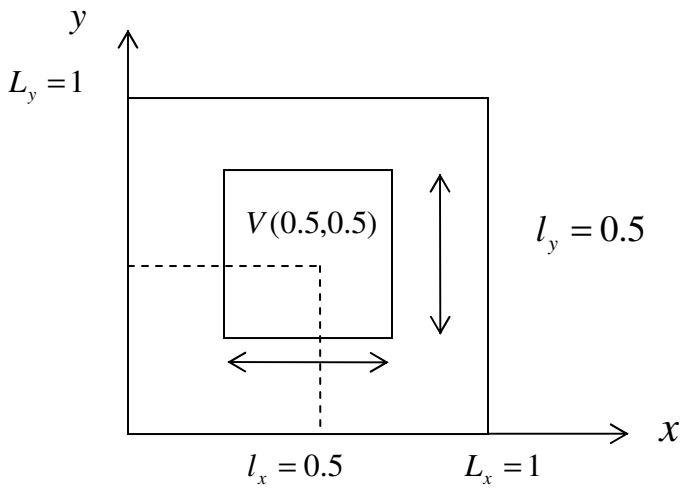

Figure 23 Geometry for testing Poisson's equation. Uniform charge density is confined to the centre square and the boundary is grounded.

The value V is calculated at the point (0.5, 0.5), as shown in Figure 23. Let $L_x = L_y = 1$ and $\rho_0 = 1$ if $0.25 < l_x < 0.75$ and $0.25 < l_y < 0.75$; otherwise, $\rho_0 = 0$. Then $A_{m,n}$ is calculated when $m =$ 0, 1, 2, 3, …1000 and $n =$ 0, 1, 2, 3, …1000.

$$A_{1,1} = (-1)^{\frac{1-1}{2}}(-1)^{\frac{1-1}{2}}1((\pi)^2 + (\pi)^2)^{-1}\frac{16}{\pi^2}\sin(\frac{\pi}{2}0.5)\sin(\frac{\pi}{2}0.5) = 0.041063929$$

$$A_{1,3} = (-1)^{\frac{1-1}{2}}(-1)^{\frac{3-1}{2}}1((\pi)^2 + (3\pi)^2)^{-1}\frac{16}{3\pi^2}\sin(\frac{\pi}{2}0.5)\sin(\frac{3\pi}{2}0.5) = 0.002737595$$

$$A_{1,5} = (-1)^{\frac{1-1}{2}}(-1)^{\frac{5-1}{2}}1((\pi)^2 + (5\pi)^2)^{-1}\frac{16}{5\pi^2}\sin(\frac{\pi}{2}0.5)\sin(\frac{5\pi}{2}0.5) = -0.000631753$$

…

After $A_{m,n}$ is calculated for different m and n, V is calculated by using Equation 4.53 and I got the value for point (0.5,0.5), $V(0.5,0.5) \approx 0.0453\text{V}$. This is an analytic solution for the value V at point (0.5, 0.5). Figure 24 shows the simulation result to calculate the Poisson's equation by using the SOR method. The value for $V(0.5,0.5) \approx 0.0465\text{V}$ if the grid points are 81 by 81. The

value changes to 0.0455V if the grid points are 401 by 401 because more grid points are being taken the value V is more accurate.

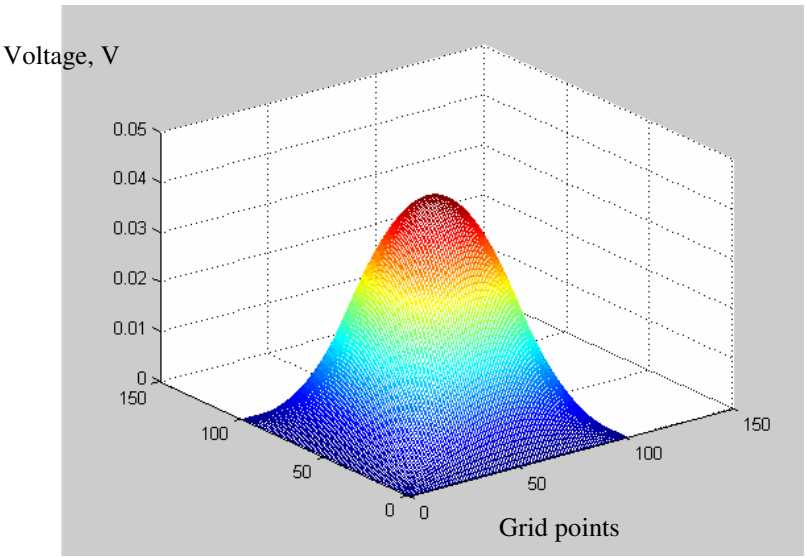

(a) 81 by 81 grid.

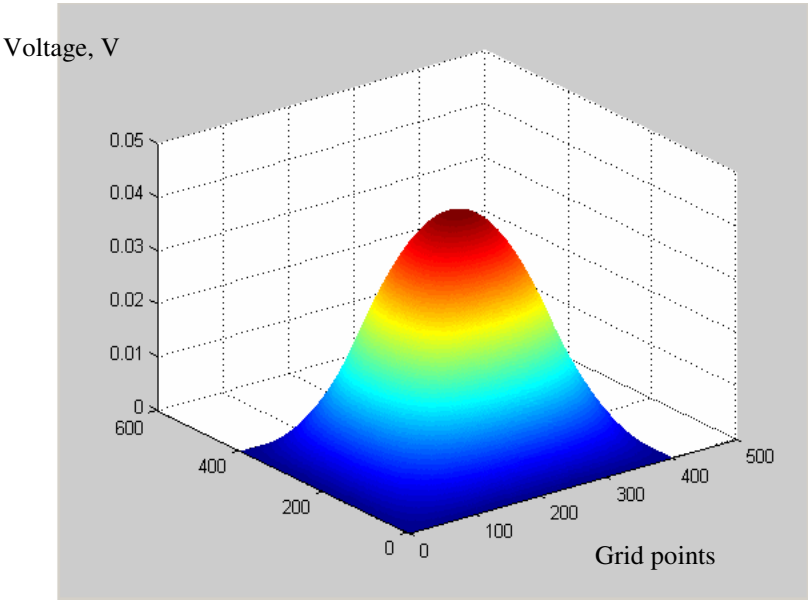

(b) 401 by 401 grid.

Figure 24 Numerical solution of Poisson's equation.

Figure 25 and Figure 26 shows the difference between simulation results and analytic solutions.

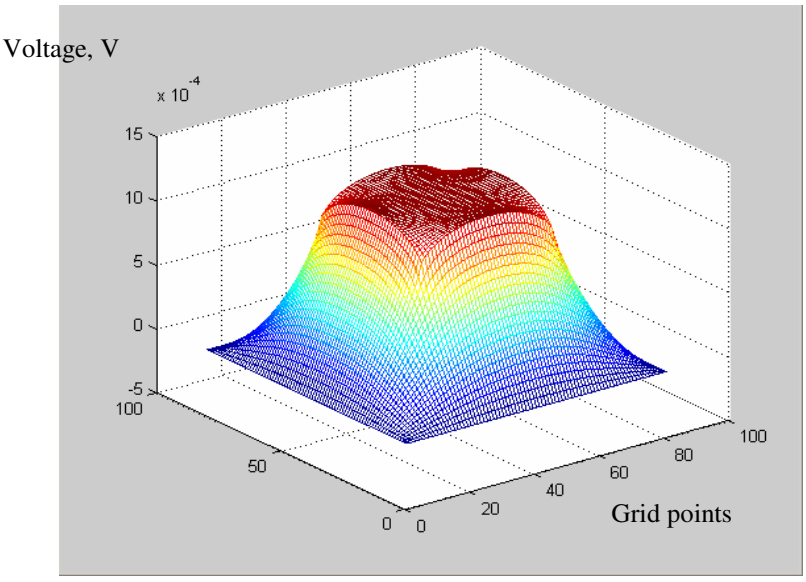

Figure 25 Difference between the numeric and analytic solutions (81 by 81 grid).

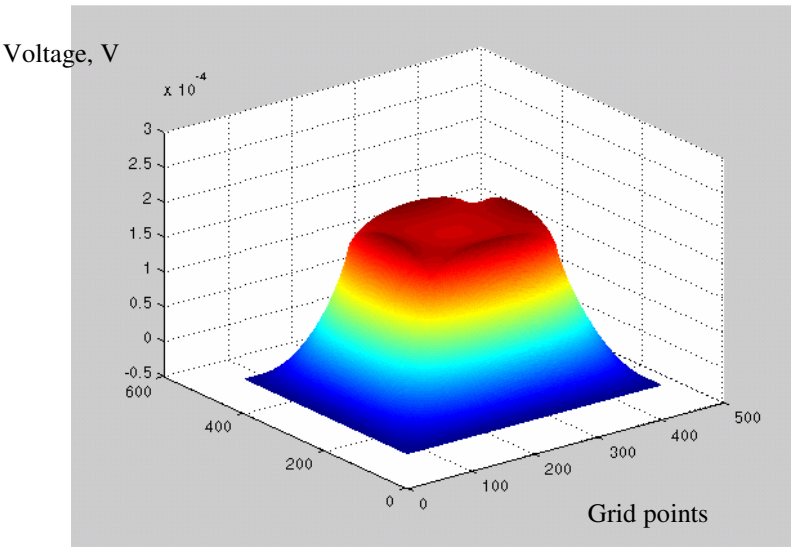

Figure 26 Difference between the numeric and analytic solutions (401 by 401 grid).

4.4 Two Dielectric Constants

The case of a boundary between two different dielectrics is solved in this section. The standard formulas (the finite different equations (Equation 4.21 and 4.23)) can not be used at the boundary between two dielectric constants since the normal component of $\vec{E}$ is discontinuous across the boundary. To derive an appropriate finite difference equation, V is expanded in a Taylor series about V_1 and V_2 to the second order and the two parabolas are matched at the boundary V_b where the slope changes by the correct ratio. The relevant cells are shown in Figure 27.

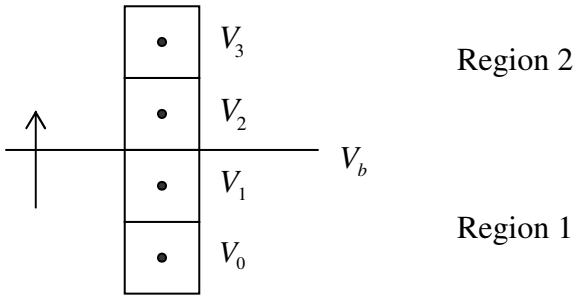

Figure 27 Boundary between two dielectric constants.

$$V(y_0+\delta y)=V(y_0)+\delta y V'(y_0)+\frac{\delta y^2}{2}V''(y_0)+... \tag{4.54}$$

Using Equation 4.54, V_0 and V_b in the Figure 27 are expanded about V_1.

$$\begin{aligned} V_0 &= V_1-\delta y V_1'+\frac{\delta y^2}{2}V_1'' \\ V_b &= V_1+\frac{\delta y}{2}V_1'+\frac{\delta y^2}{8}V_1'' \end{aligned} \tag{4.55}$$

Expanding about V_2, then

$$V_3 = V_2 + \delta y V_2' + \frac{\delta y^2}{2} V_2''$$
$$V_b = V_2 - \frac{\delta y}{2} V_2' + \frac{\delta y^2}{8} V_2'' \tag{4.56}$$

Let us consider the y component of the electric field. It is given by

$$E_y = -\frac{\partial V}{\partial \delta y} = -V'(y_0) - \delta y V''(y_0) \tag{4.57}$$

At the boundary in region 1 (Figure 27), Equation 4.57 becomes

$$E_y^- = -V_1' - \frac{\delta y}{2} V_1'' \tag{4.58}$$

At the boundary in region 2 (Figure 27), Equation 4.57 becomes

$$E_y^+ = -V_2' + \frac{\delta y}{2} V_2'' \tag{4.59}$$

Now, I put Equation 4.58 and Equation 4.59 into the boundary condition. $\varepsilon_1 E_y^- = \varepsilon_2 E_y^+$. It gives

$$\varepsilon_1 V_1' + \varepsilon_1 \frac{\delta y}{2} V_1'' = \varepsilon_2 V_2' - \varepsilon_2 \frac{\delta y}{2} V_2'' \tag{4.60}$$

Using Equation 4.55, 4.56 and Equation 4.60, V_1'' and V_2'' are solved.

$$V_1'' = \frac{1}{\delta y^2} \frac{1}{(\varepsilon_1 + \varepsilon_2)} [V_0 (\frac{4}{3}\varepsilon_2 + \varepsilon_1) - \frac{1}{3}\varepsilon_2 V_3 - (4\varepsilon_2 + \varepsilon_1) V_1 + 3\varepsilon_2 V_2] \tag{4.61}$$

$$V_2'' = \frac{1}{\delta y^2} \frac{1}{(\varepsilon_1 + \varepsilon_2)} [-\frac{1}{3}\varepsilon_1 V_0 + (\frac{4}{3}\varepsilon_1 + \varepsilon_2) V_3 - (4\varepsilon_1 + \varepsilon_2) V_2 + 3\varepsilon_1 V_1] \tag{4.62}$$

4.4.1 Testing of the Boundary between Dielectrics

For example, two dielectric constant are given, $\varepsilon_1 = 2$ when $y \le 0.25$, $\varepsilon_2 = 1$ when $0.25 < y \le 1$ and $\rho_0 = 1$. The SOR method is used to solve the potential at each point and get values for V_0, V_1, V_2 and V_3 ($V_0 = 0.0385V$, $V_1 = 0.0377V$, $V_2 = 0.0368V$, $V_3 = 0.0356V$, $\Delta y = 1$). Equation 4.61 and Equation 4.62 are used to solve V_1'' and V_2''. Then Equation 4.55, 4.56, V_1'' and V_2'' are used to solve V_b. I get $V_b = 0.0374V$. Therefore,

$$\frac{E_{y1}}{E_{y2}} = \frac{\dfrac{V_b - V_2}{\Delta y}}{\dfrac{V_1 - V_b}{\Delta y}} = \frac{0.0006}{0.0003} = 2 = \frac{\varepsilon_1}{\varepsilon_2}$$

Figure 28 shows the simulation result for the electric field along the y direction. From the simulation result, I got $E_{y1} = 0.0759$ and $E_{y2} = 0.0390$.

$$\frac{E_{y1}}{E_{y2}} = \frac{0.0759}{0.0390} = 1.946 \approx \frac{\varepsilon_1}{\varepsilon_2}$$

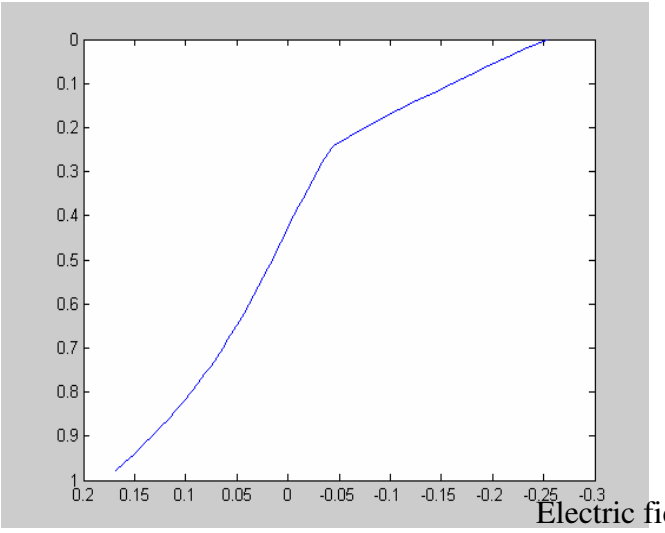

Figure 28 The electric field along y direction.

4.6 Boundary Conditions

The three main equations–Poisson's equation, the current equation and the continuity equation–have been discussed in previous section. These equations are solved numerically with the appropriate boundary conditions in order to obtain the charge density profile in the TFT. The first and the last box in a row are the boundaries (A_1 and A_N, respectively), as shown in Figure 29.

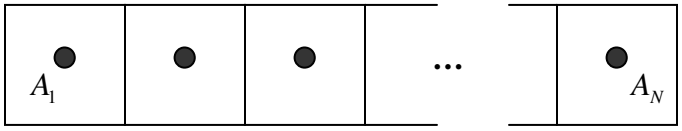

Figure 29 Boundaries of the grid.

The first and the last box can be either a metal or an insulator material. Different materials affect the current flow. Therefore, the current equation and the continuity equation are also affected. If no current flows through the material, an insulator material can be used at the boundary, and it doesn't matter if the boundary boxes connect to the wire since no electrons or holes cross the boundary boxes (A_1, A_N). Electron or hole current density equals to zero at the boundary.

If metal is used for the boundary boxes, the metal material allows the electrons or holes to cross when there is a current flow. The boundary boxes can provide unlimited numbers of electrons since the metal acts as an electron reservoir. The current equations have been mentioned in the previous section, which includes two parts: the drift current equation and the diffusion current equation. I assume the current only depends on the drift current equation and the diffusion current equals zero at the boundary boxes. Then the current Equation 4.10 and Equation 4.11 are reduced to

$$\vec{J}_e = qn\mu_e\vec{E} \tag{4.63}$$

$$\vec{J}_h = qp\mu_h\vec{E} \tag{4.64}$$

The continuity equations are not used to calculate the change of electrons or holes in the boundary boxes because the boundary boxes provide unlimited numbers of electrons or holes. So I assume the boundary boxes are not affected by the neighboring boxes and maintain a constant number of electrons or holes. If the neighboring box transfers some electrons or holes to the boundary boxes, the number of electrons or holes in the boundary boxes doesn't change. If the neighboring boxes need to receive an amount of electrons or holes from the boundary boxes without changing the number in the boundary boxes.

4.7 Flow Chart

Figure 30 shows the calculation sequence for the thin film transistor simulation and the relation among the three main equations: Poisson's equation, the current equation and the continuity equation. The flow chart gives a general idea how the simulation works.

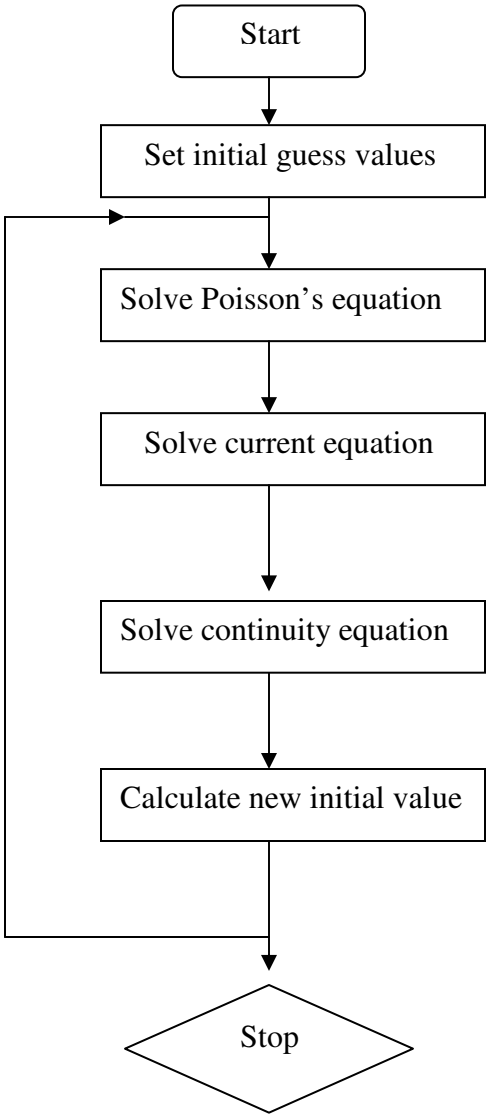

Figure 30 Flowchart.

4.8 Normalized Noise Power Spectral Density in the Channel of a FET

The channel of a FET is divided into cells, as shown in Figure 31. The charge density of each cell is obtained from the previous simulation process. The normalized noise power spectral density of each cell is calculated from the charge density. Then the total normalized noise power spectral density in the channel of a FET is calculated, based on the normalized noise power spectral density of each cell.

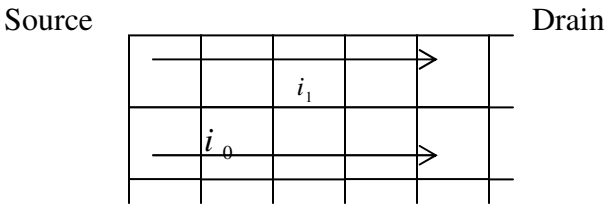

Figure 31 Grid points in the channel of a FET.

The first step is to obtain the noise of each cell from the charge densities. Thus noise must be obtained either from experiments on a-Si:H or from a theory. However, either way it is obtained the noise can be characterized by the Hooge relation. The normalized noise power density is obtained by dividing the power spectral density of the resistance fluctuations (S_r) by the square of the resistance (R_0). The Hooge relation (Equation 2.14) gives

$$S_n = \frac{\overline{S_r(\omega)}}{R_0^2} = \frac{\alpha_H}{N_{total}|f|} \tag{4.65}$$

where N is the number of charge carriers, which is determined by the free carrier densities (n, p). That is

$$N = \Delta x \Delta y w (n + p) \tag{4.66}$$

where Δx and Δy are the cell dimensions and w is the width of the FET in the third dimension. The value of α_H is what must be determined through experiment or a microscopic theory.

Now, let us consider each cell as an independent fluctuating resistor, the normalized noise power spectra of each cell ($S_{n(cell)}$) is also obtained by dividing the square of the drain source current fluctuations of each cell by the square of the drain source current of each cell . $S_{n(cell)}$ is given by

$$S_{n(cell)} = \frac{(\delta I)^2}{I^2} = \frac{(\delta V)^2}{V^2} = \frac{(\delta R)^2}{R^2} = \frac{(\delta G)^2}{G^2} \tag{4.67}$$

where $\delta I, \delta V, \delta R, \delta G$ are the fluctuations in current I, voltage V, resistance R or conductance G. The normalized noise power density of each cell is calculated using

$$S_{n(cell)} = \frac{(\delta R)^2}{R^2} = \frac{(\delta G)^2}{G^2} = \frac{\alpha_H}{Nf} \tag{4.68}$$

In the channel of the FET, the current flows in the x direction, as shown in Figure 31. Each cell is treated as an independent resistor which is connected in series in each row. And each row j (separate series of resistors) is connected in parallel to form the channel of a FET.

For a set of resistors connected in series as shown in Figure 32, the total resistance is the summation of each resistor in the series. Then the resistance for each horizontal slice of the FET is

$$R_j^{row} = \sum_{i=1}^{M} R_{ij} \tag{4.69}$$

where M is the number of resistors.

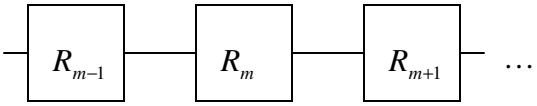

Figure 32 Resistors connected in series.

Let δR_{ij} be the magnitude of the fluctuations in the resistance R of the cell (i, j) in the channel of a FET and assume that the fluctuations in the resistors are uncorrelated. The fluctuations in the total resistance of the chain of resistors are deduced from Equation 2.28,

$$\delta R_j^{row} = [\sum_{i=1}^{M} (\delta R_{ij})^2]^{1/2} \tag{4.70}$$

Putting Equation 4.69 and 4.70 into Equation 4.67, yields the normalized noise power of the whole chain

$$S_{n_{series}} = \frac{(\delta R_j^{row})^2}{(R_j^{row})^2} = \frac{\sum_{m=1}^{M} \delta R_{ij}^{\ 2}}{(\sum_{m=1}^{M} R_{ij})^2} \tag{4.71}$$

Now, consider the separate series of resistors connected in parallel. Here it is easier to work with conductance which will be converted to resistance later. For set of conductors connected in parallel, as shown in Figure 33, the total conductance in the channel of the FET is

$$G_{total} = \sum_{n=1}^{N} G_n \tag{4.72}$$

where N is the number of conductors.

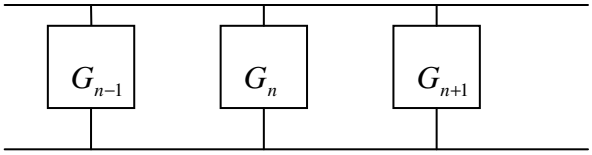

Figure 33 Conductors connected in parallel.

Let the fluctuations in G_n be δG_n; then the total conductance has fluctuations given by

$$\delta G_{tot} = (\sum_{n=1}^{N} \delta G_n^2)^{1/2} \tag{4.73}$$

Putting Equation 4.72 and 4.73 into Equation 4.67, yields the normalized noise power density

$$S_{n_{total}} = \frac{(\delta G_{tot})^2}{G_{tot}^2} = \frac{\sum_{n=1}^{N} \delta G_n^2}{(\sum_{n=1}^{N} G_n)^2} \tag{4.74}$$

Therefore, the total normalized noise power of the FET is

$$S_{n_{total}} = \frac{\sum_{j=1}^{N} (\delta G_j^{row})^2}{(\sum_{j=1}^{N} G_j^{row})^2} \tag{4.75}$$

where the conductance of each horizontal slice of the FET is

$$G_j^{row} = (\sum_{i=1}^{M} R_{ij})^{-1} \tag{4.76}$$

Now, we need to convert the $(\delta G_j^{row})^2$ into $(\delta R_j^{row})^2$ in order to use the Equation 4.75 to calculate the total noise. Notice that

$$S_n = \frac{(\delta R)^2}{R^2} = \frac{(\delta G)^2}{G^2}$$

That implies

$$\delta G^2 = \frac{G^2}{R^2}(\delta R)^2 = G^4(\delta R)^2 \tag{4.77}$$

And thus

$$(\delta G_j^{row})^2 = (G_j^{row})^4 (\delta R_j^{row})^2 \tag{4.78}$$

From the Equation 4.68

$$(\delta R_{ij})^2 = \frac{\alpha_H}{f}\frac{R_{ij}^2}{N_{ij}} \tag{4.79}$$

Inserting the Equation 4.79 into the Equation 4.70 gives

$$\delta R_j^{row} = [\sum_{i=1}^{M} \frac{\alpha_H}{f}\frac{R_{ij}^2}{N_{ij}}]^{1/2} \tag{4.80}$$

In order to evaluate Equation 4.80, R_{ij} and N_{ij} need to be obtained from the simulation. Resistance is the inverse of conductance, that is

$$R_{ij} = \frac{1}{G_{ij}} \tag{4.81}$$

where the conductance G_{ij} is determined by the conductivity σ_{ij} of a cell (i, j), that is

$$G_{ij} = \frac{w\Delta y}{\Delta x}\sigma_{ij} \tag{4.82}$$

Conductivity σ_{ij} is calculated by

$$\sigma_{ij} = qn_{ij}\mu_e + qp_{ij}\mu_h \tag{4.83}$$

where n_{ij} and p_{ij} are the free electron and hole carrier densities, μ_e and μ_h are the electron and hole drift mobilities. Therefore, all the unknowns from the Equation 4.75 are solved, and the normalized noise power spectral density in the channel of a FET can be calculated from the simulation results.

5 SIMULATION RESULTS AND DISCUSSION

This chapter discusses the simulation results and data analysis. First, the dependencies of the simulated drain-source current on the drain-source voltage and gate voltage are determined in order to verify that the simulated FET works properly. Then the simulation results are compared to the experimental data. Finally, the magnitude of the noise power is calculated from the simulation. The effects of the drain-source voltage, drain-source current and gate voltage on the noise spectrum are compared to the experimental data.

5.1 Simulation Results and Data Analysis

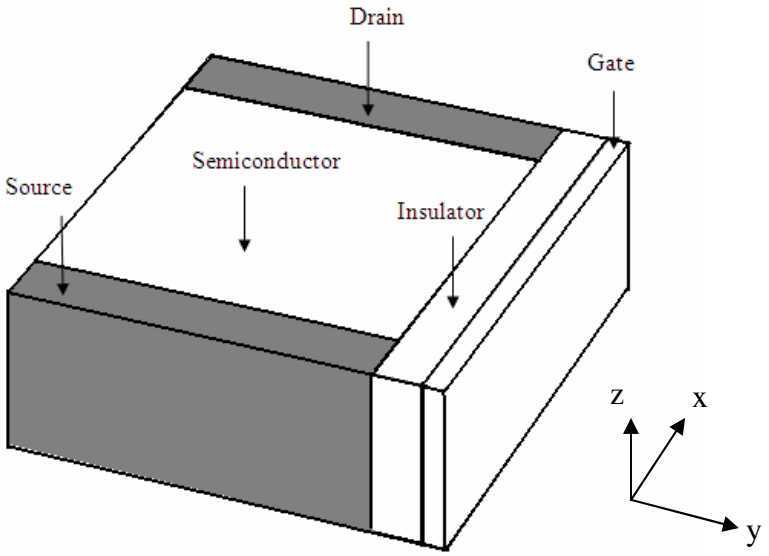

Figure 34 Three dimensional geometry of the FET.

The three dimensional geometry of the FET is shown in Figure 34; the simulation suppresses the width (z direction). With no voltage applied to the gate ($V_g = 0\text{V}$), the region from the source to the drain is an $n^+ \; n_i \; n^+$ structure. The source and the drain are isolated by a low conductivity region. An n-channel does not form, and no current can flow, as shown in Figure 35 and Figure 36.

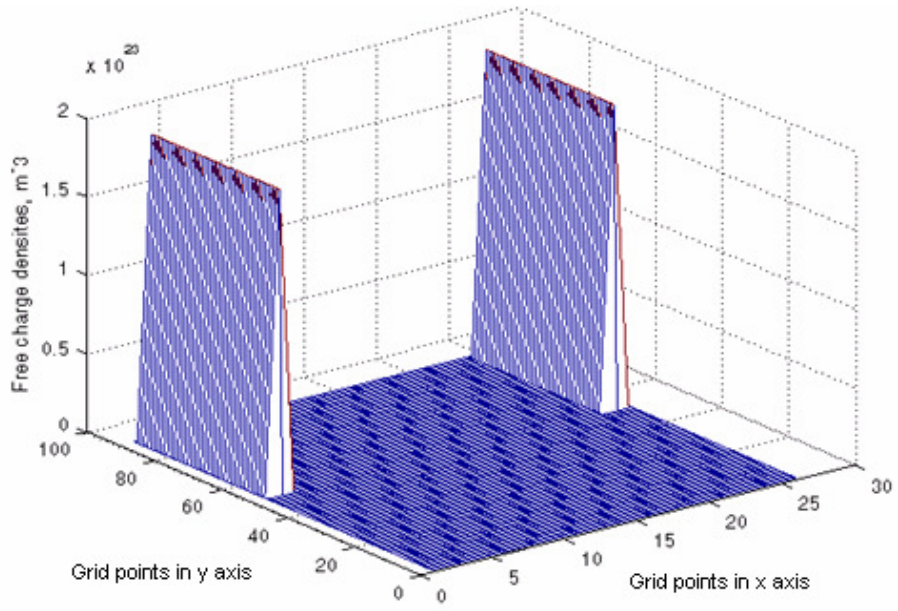

Figure 35 Free charge densities in the FET when $V_g = 0\text{V}$ and $V_{ds} = 0\text{V}$ for a simulated time of 4.8μs.

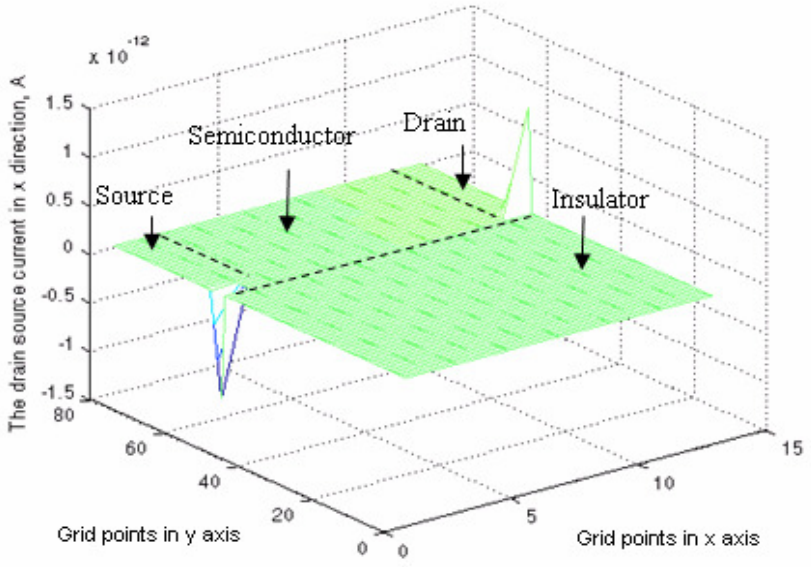

Figure 36 The drain-source current when $V_g = 0\text{V}$ and $V_{ds} = 0\text{V}$ for a simulated time of 4.8μs.

Figure 36 shows that the magnitude of I_{ds} equals $7\times10^{-13}\text{A}$ at the boundaries between the insulator and two n^+ regions, and I_{ds} equals 0A between the source and the drain. Later, when different gate voltages and drain-source voltages were applied, simulation result gave the

magnitude of I_{ds} in the range of 0.01×10^{-6}A and 0.2×10^{-6}A. Therefore, the magnitude of current (7×10^{-13}A) is small enough to ignore, and no current flows. When a positive voltage was applied to the gate ($V_g > 0$V), an n-channel accumulation layer was formed under the gate after a relaxation time (see below) and linked the two n^+ regions of source and drain, as shown in Figure 38.

The relaxation time is used to determine if an equilibrium condition has been reached. We can estimate the relaxation time using two methods. In the first method, I consider the n-channel accumulation layer as a capacitor with a capacitance of 19nF/cm^2 connected in series with a 21.1MΩ resistor. The capacitance is calculated using the depth of the insulator, the width and the length of the FET. The resistance is calculated using the charge densities from the simulation results, the width and the length of the FET. Then, the relaxation time τ requires charging the capacitor through the resistor equals 9.7μs or the simulation requires 9.7μs forming the n-channel accumulation layer. In addition, for comparison purposes, I used the physical size of the FET from the previous experiment (width = 100μm and length = 50μm). In the second method, the relaxation time τ can be calculated using the experimental results. In the previous experiment a 19nF/cm^2 capacitor was used [25], and the resistance was 22.5MΩ which was calculated using I_{ds} and V_{ds} from the experimental results (Figure 47). The relaxation time τ equals 9.96μs. Therefore, both methods yield similar relaxation times.

Figure 37 shows an example of the magnitude of I_{ds} versus the simulated time t. When $V_g = 15$V and $V_{ds} = 5$V, the magnitude of I_{ds} from the simulation results is 4.02×10^{-8}A after the program was run for 490,000 time steps, where each time step is one time through the loop in Figure 30, and $t = 10$μs. The magnitude of I_{ds} from the simulation results changes to 4.83×10^{-8}A after the program was run for 1,280,000 time steps and $t = 21$μs. The magnitude of I_{ds} is not constant in the time interval (10μs to 21μs); the magnitude of I_{ds} changes by 25%. Although I_{ds} would likely continue to change, it is reasonable to assume that the profile of the channel is well established at least for the purpose of calculating the noise.

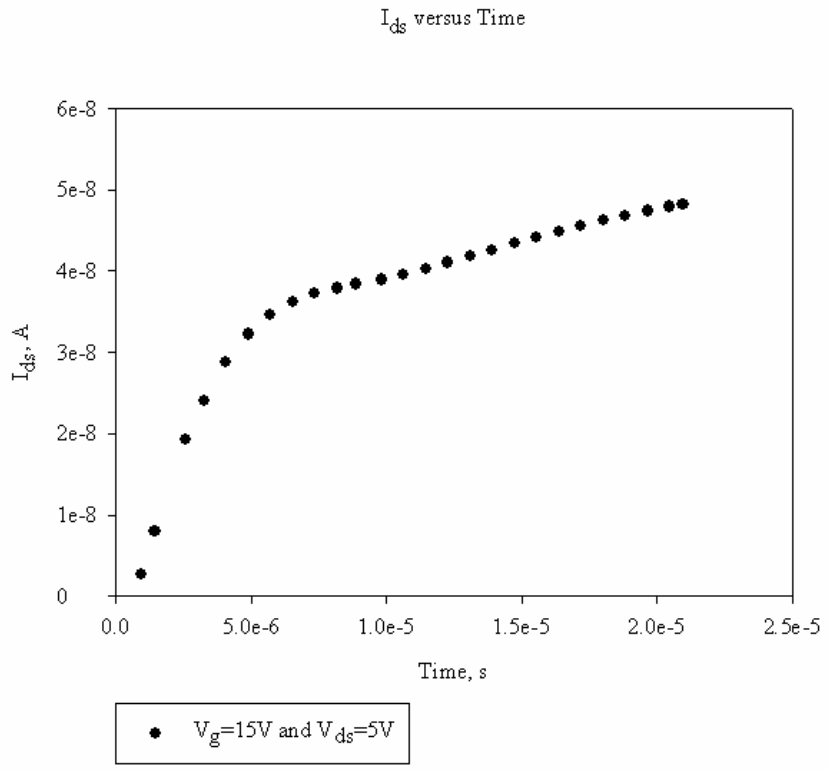

Figure 37 Magnitude of the drain-source current versus simulated time for grid of 26 x 90.

Figure 38 and 39 show the free charge densities of the FET along the x-axis and y-axis when $V_g = 10\text{V}$ and $V_{ds} = 0\text{V}$ after a simulated time of $18.8\mu\text{s}$. The simulation was run for $18.8\mu\text{s}$ which is much longer than the relaxation time τ. Therefore, an equilibrium condition is reached and an n-channel accumulation layer is formed. The size of the n-channel ($\text{length} = 46\mu\text{m}$ and $\text{depth} = 33.9\text{nm}$) is calculated by multiplying the number of grid-cells with the unit cell dimensions ($\text{length} = 2\mu\text{m}$ and $\text{depth} = 11.3\text{nm}$).

Figure 40 shows the simulation results for the magnitude of I_{ds} under the gate when $V_g = 10\text{V}$ and $V_{ds} = 0\text{V}$ for a simulated time of $18.8\mu\text{s}$. Since the drain-source voltage is equal to zero ($V_{ds} = 0\text{V}$), no current flows. The magnitude of I_{ds} from the results of the simulation is $4\times10^{-10}\,\text{A}$ which flows from n^+ regions to n region, but the magnitude is small enough to ignore.

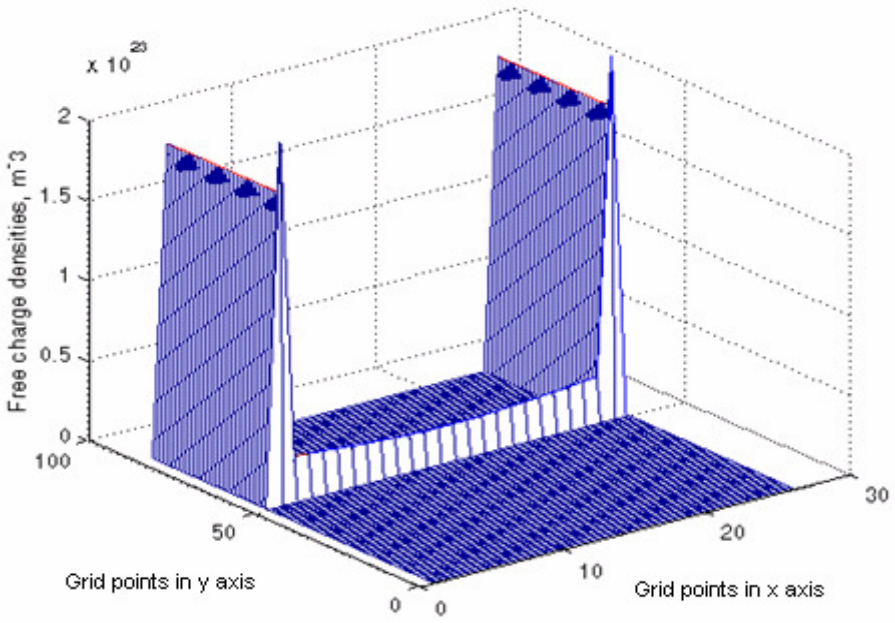

Figure 38 Free charge densities of the FET when $V_g = 10\text{V}$ and $V_{ds} = 0\text{V}$ for a simulated time of 18.8μs.

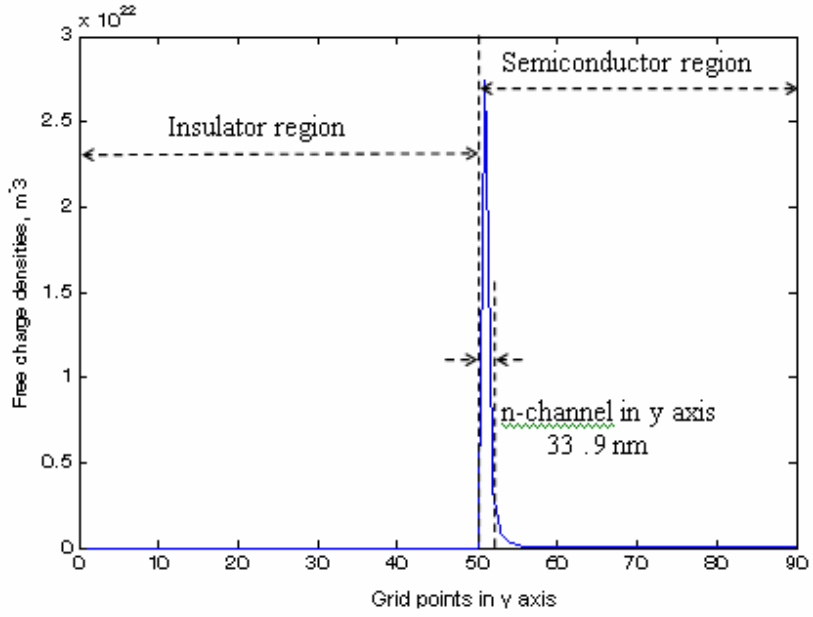

Figure 39 Free charge densities in y direction for a simulated time of 18.8μs at the midpoint between the source and the drain.

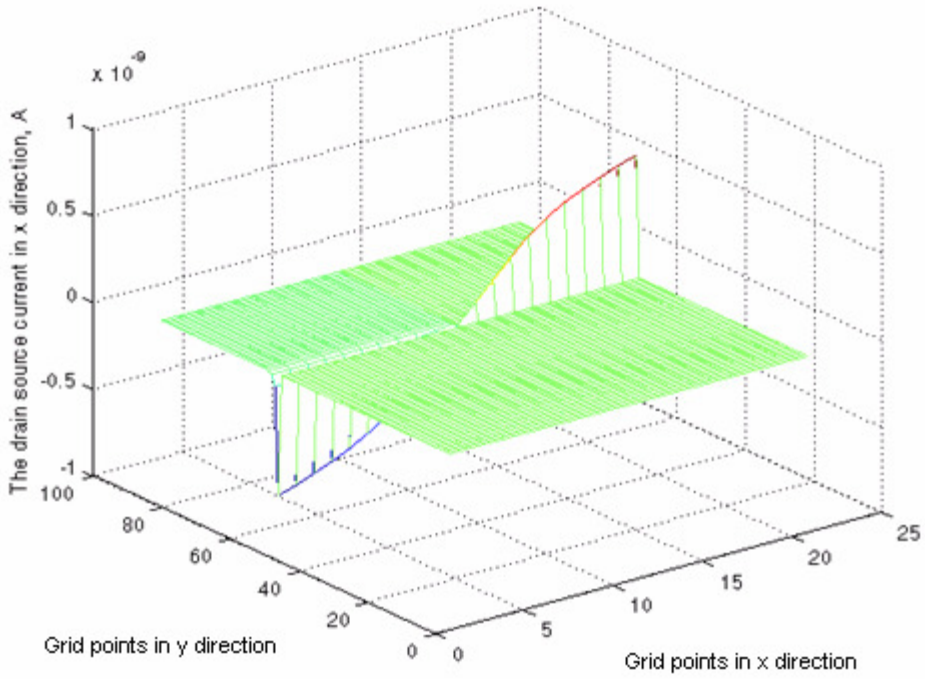

Figure 40 The drain-source current under the gate when $V_g = 10\text{V}$ and $V_{ds} = 0\text{V}$ for a simulated time of 18.8μs.

As soon as the drain-source voltage increases ($V_{ds} > 0\text{V}$), the drain-source current flows and increases rapidly with the drain-source voltage, as shown in Figure 41 and 46. The voltage along the channel varies from zero at the source end to V_{ds} at the drain, as shown in Figure 42. There are two regions (region 1 and region 2) in Figure 42 which show the voltage increases or decreases rapidly because of the built-in potential between n and n^+ regions.

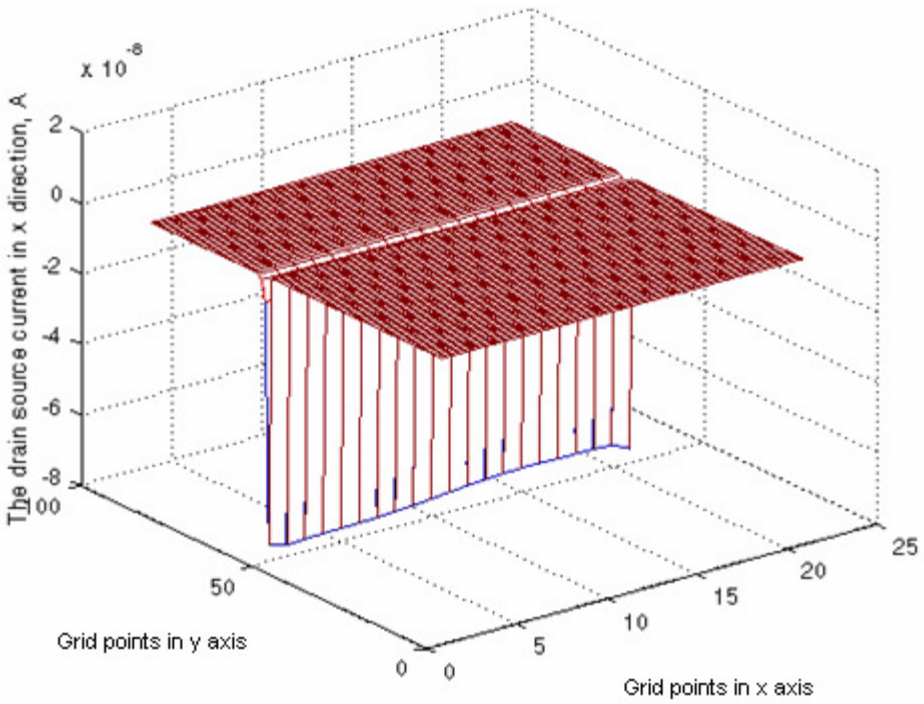

Figure 41 The drain-source current when $V_g = 15\text{V}$ and $V_{ds} = 10\text{V}$ for a simulated time of 16.5μs.

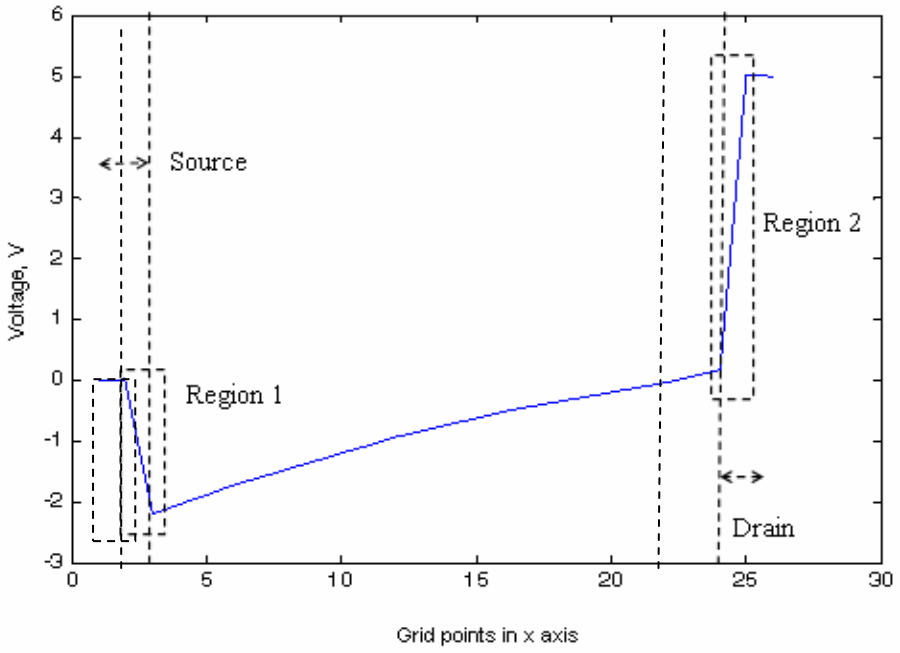

Figure 42 The voltage along the channel for $V_{ds} = 5\text{V}$ for the cells adjacent to the insulator.

The channel of the FET is divided into cells, and the pinch off point can be determined using the charge densities from the simulation results, as shown in Figure 43 and 45. Therefore, I can count number of the cells to calculate the length of the accumulation region of the channel. Increasing V_{ds} narrows the channel towards the drain, as shown in Figure 45. The resistance of the n-channel increases with the drain-source voltage. Therefore, the drain-source current does not increase linearly with the drain-source voltage.

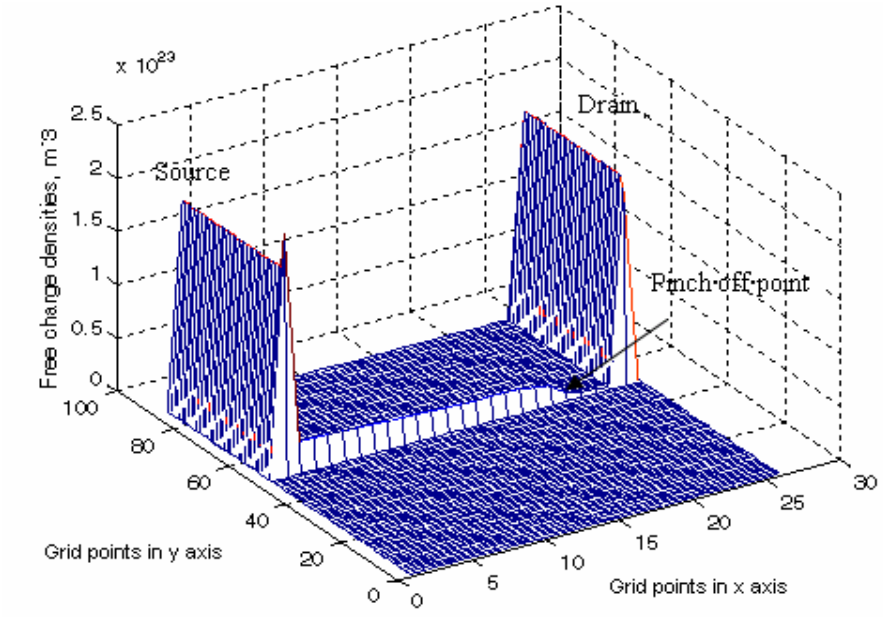

Figure 43 Simulation results charge densities when $V_{ds} = 13\text{V}$ and $V_g = 10\text{V}$ for a simulated time of 18.2μs.

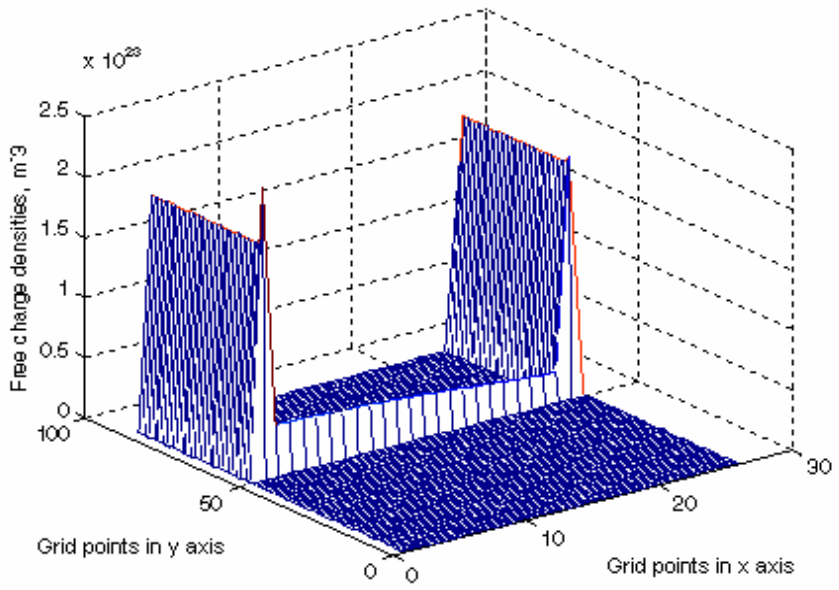

Figure 44 Simulation results charge densities when $V_{ds} = 13\text{V}$ and $V_g = 15\text{V}$ for a simulated time of 1.9μs.

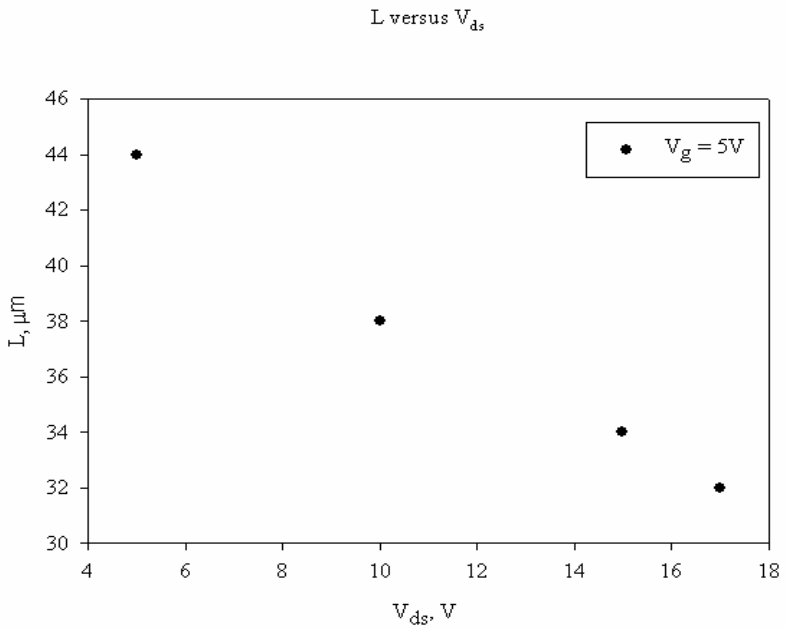

Figure 45 The length of the accumulation region of the channel versus V_{ds} for $V_g = 5\text{V}$ (simulated time varied from 16.4μs to 29μs depending on the run).

Figure 46 shows the magnitude of I_{ds} versus V_{ds} when different gate voltages (5V, 10V, 13V, 15V, 16V, 18V) are applied; and simulation times ranged from 20μs to 25μs. As shown in Figure 46, increasing V_{ds} leads to a sub-linear increase in I_{ds}. For a constant V_{ds}, increasing V_g increases I_{ds} because I_{ds} increases mainly due to the larger number of electrons in the channel; however, the pinch off point also moves, as shown in Figure 43 and 44.

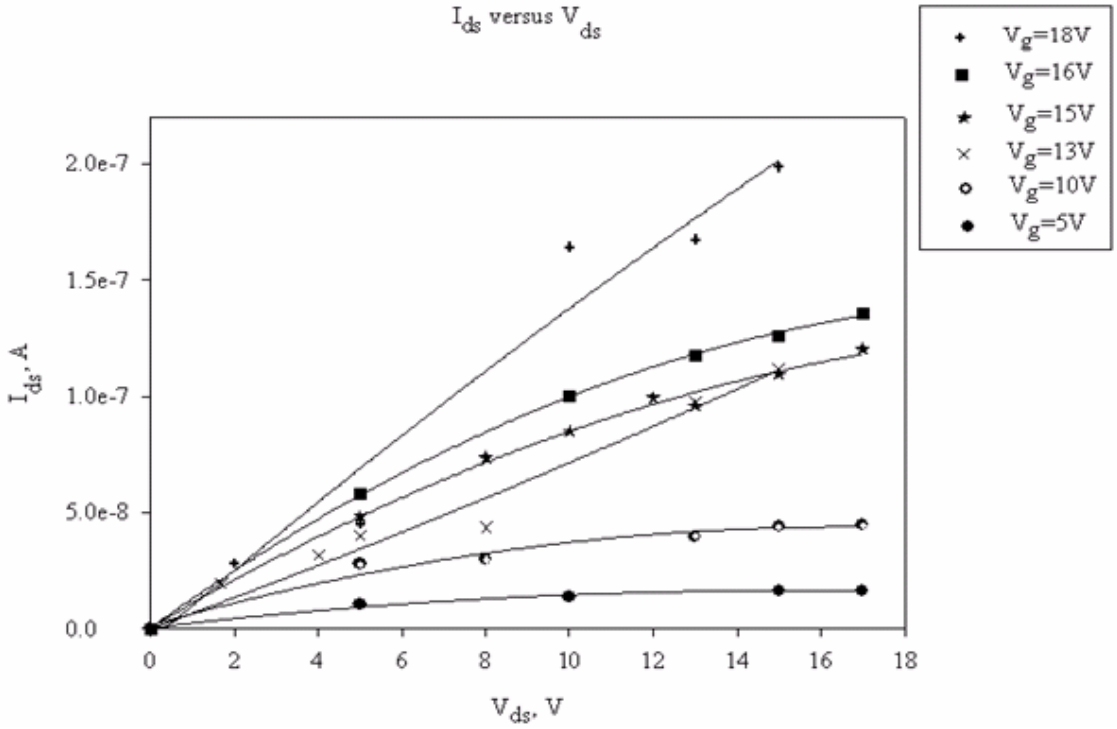

Figure 46 Simulation results I_{ds} versus V_{ds} for different gate voltages (simulated times from 20μs to 25μs).

In addition, I used computer software called SigmaPlot to plot the "best fit" curve of the data points. I will have more accurate curve if more points are used. However, only five points were used to plot each curve in Figure 46. Therefore, one value can influence the curve's overall shape. In Figure 46, a few points are not accurate because the simulation was not run long enough. For example, when $V_{ds} = 15\text{V}$ and $V_g = 18\text{V}$, the magnitude of drain-source current is larger than the excepted value. Therefore, the curve shape for $V_g = 18\text{V}$ does not look right.

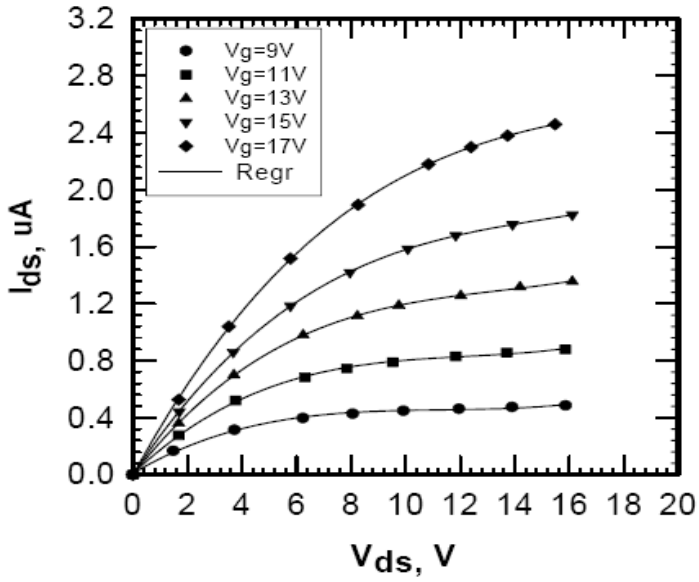

Figure 47 Experimental results I_{ds} versus V_{ds} for different gate voltages [7].

Figure 47 shows the experimental relationship between I_{ds} and V_{ds}, and the shapes of experimental curves are similar to the simulation ones. However, the magnitude of I_{ds} from the experimental results is 20 times larger than the simulation results. Figure 48 shows a comparison between the simulation results and the experimental results when $V_g = 15\text{V}$. Multiplying the simulation results by 20 gives a curve close to the experimental curve. The difference between the simulation and the experimental results is due to the following reason. The electron drift mobility ($\mu_e = 1\times10^{-4}\,\text{m}^2/\text{Vs}$) is used in the simulation. However, the electron drift mobility value for the hydrogenated amorphous silicon material is $1\times10^{-3}\,\text{m}^2/\text{Vs}$ which is 10 times larger than the simulation electron drift mobility [20]. The total current density is the sum of the drift current density and the diffusion current density, and the drift current density depends on four parameters: the electric field, the electron or hole concentration, the mobility constant, and the charge. Therefore, I believe the drift mobility value scales the drift current and the magnitude of I_{ds} will become 10 times lager if $1\times10^{-3}\,\text{m}^2/\text{Vs}$ is used in the simulation. Whereas this might have a minor effect on the distribution of charge in the channel, the relative changes with applied

voltage should not change much and thus the drain cures should to a reasonable approximation simply scale with the drift mobility.

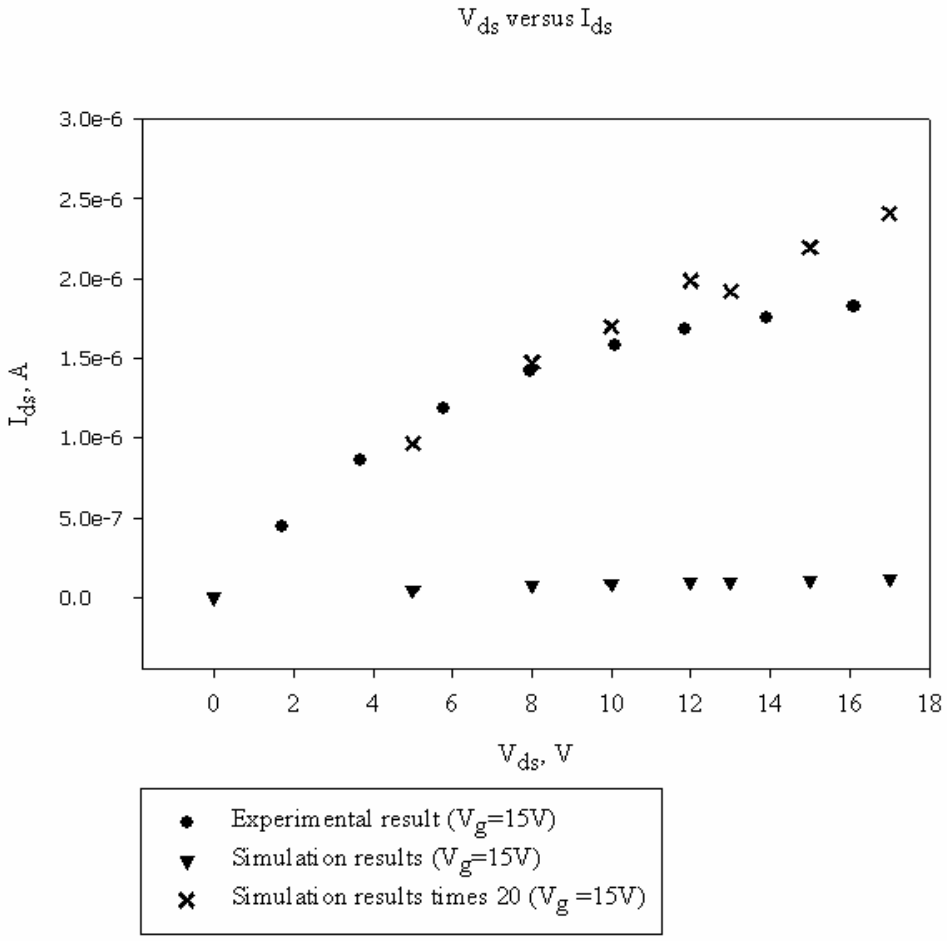

Figure 48 Magnitude of I_{ds} from the experimental and the simulation results when $V_g = 15\text{V}$ (simulated times range from $8\mu\text{s}$ to $27\mu\text{s}$).

Figure 49 shows the magnitude of the drain-source currents versus the gate voltages when different drain-source voltages are applied (0V, 5V, 8V, 10V, 13V, 15V, 17V). As shown in Figure 49, when $V_{ds} = 0\text{V}$, I_{ds} is not affected by V_g and no current flows. Increasing V_{ds} ($V_{ds} > 0\text{V}$), the current flows and increases with V_g. Increasing V_{ds} leads to an nonlinear

increases in I_{ds}, as shown in Figure 49. Figure 49 also shows I_{ds} increases with V_{ds} when the same V_g is applied to the gate. Figure 50 gives the relation between I_{ds} and V_{ds} when $V_g = 15\text{V}$.

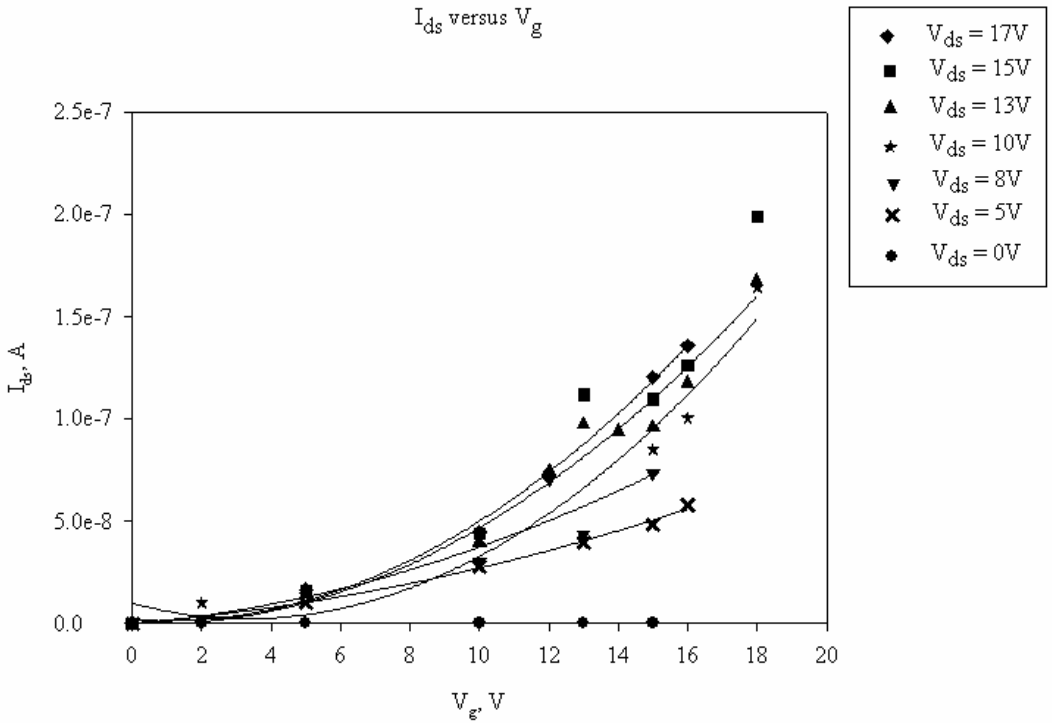

Figure 49 Simulation results for I_{ds} versus V_g (simulated times from $20\mu\text{s}$ to $25\mu\text{s}$).

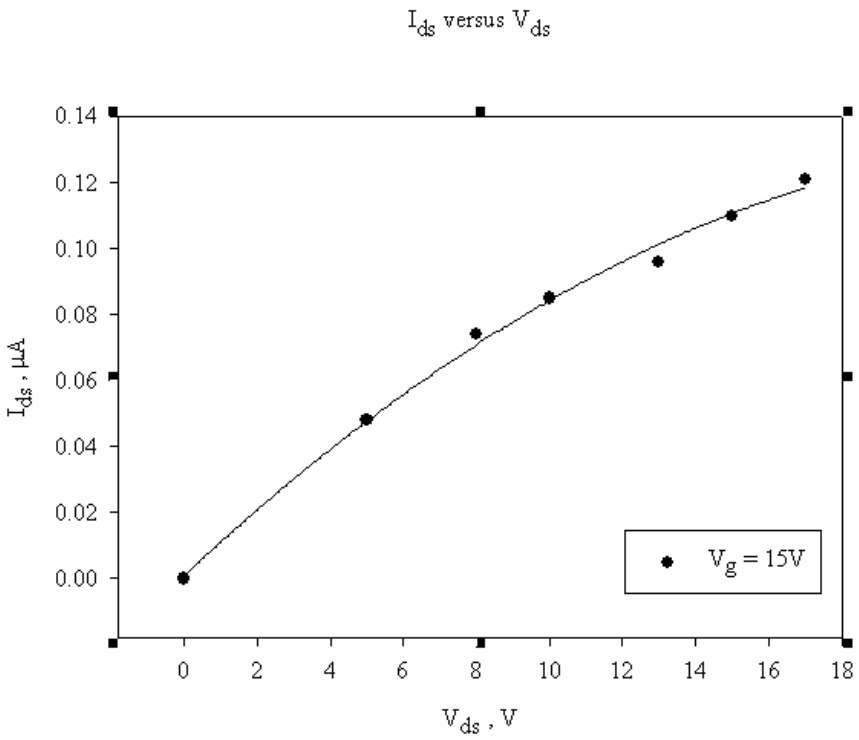

Figure 50 Magnitude of I_{ds} versus V_{ds} when $V_g = 15\text{V}$ (simulated times from 9μs to 25μs).

Figure 51 gives the simulation results for the square root of current density versus the gate voltage when different gate voltages are applied. Figure 51 shows that the magnitude of $(I_{ds})^{1/2}$ increases linearly with V_g and satisfies the equation [14]

$$I_{ds} = \frac{\mu C_i W}{2L}(V_g - V_{th})^2 \tag{5.1}$$

where μ is the field effect mobility, C_i is the gate insulator capacitance per unit area, W is the channel width, L is the channel length, and V_{th} is the threshold voltage. When $V_g = 15\text{V}$, $V_{ds} = 15\text{V}$, $\mu = 1\times10^{-4}\,\text{m}^2/\text{Vs}$, $C_i = 19\text{nF/cm}^2$, $L = 44\mu\text{m}$, $W = 100\mu\text{m}$ and $V_{th} = 12\text{V}$, I get $I_{ds} = 0.19\mu\text{A}$. However, the simulation result was $I_{ds} = 0.11\mu\text{A}$ which is smaller than the theoretical result. The magnitude of current may become larger if the simulation runs longer, as shown in Figure 37. However, it is close enough for noise calculations. The simulation of the

FET agrees reasonably well with the experimental data (Figure 46 and Figure 47). I have confidence that the FET is being simulated properly and I can proceed to calculate the noise.

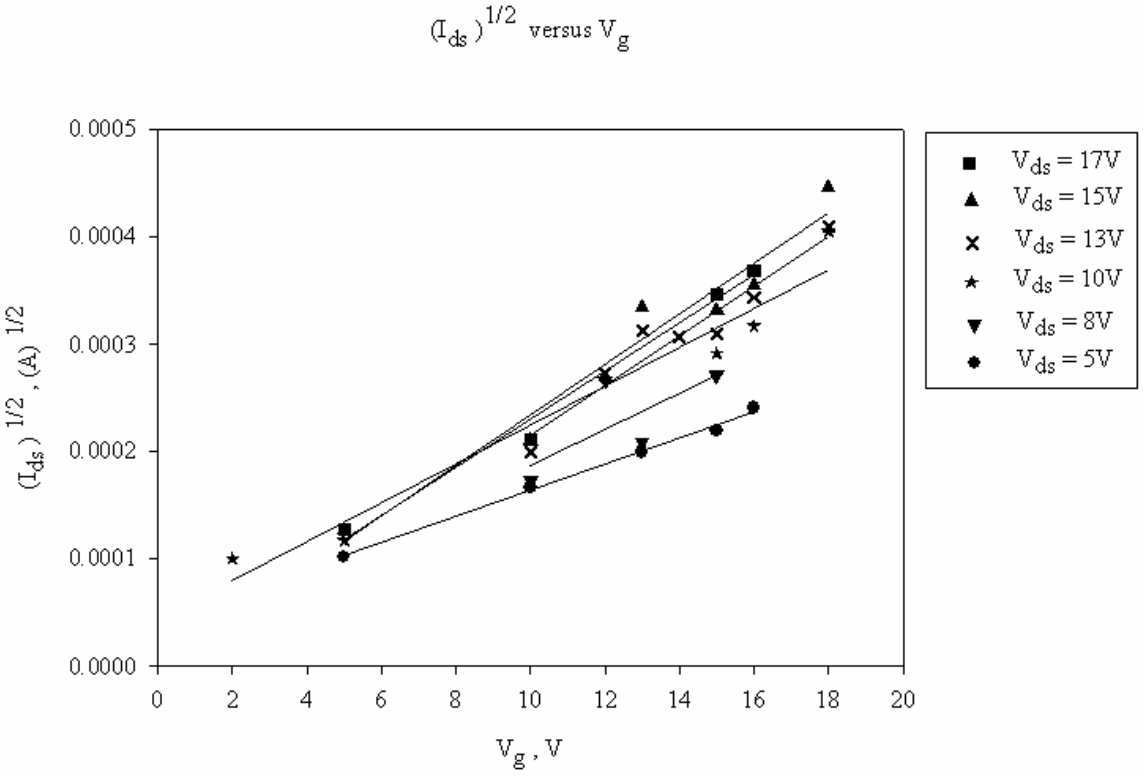

Figure 51 Simulation results $(I_{ds})^{1/2}$ versus V_g (simulated times from 20μs to 25μs**).**

5.2 The Effect of Drain-Source Voltage on Noise Spectrum

For a given gate voltage, the normalized noise spectra are calculated at several drain-source voltages from 5V to 17V. The noise values are calculated by Equation 4.75. The effective channel length changes by a shift of the pinch off point. It is easy to derive the relation between the normalized noise power and the channel length. Consider the channel length L that has a certain amount of resistance noise S_R, and the resistance of the channel is R; therefore, the normalized noise power is $\frac{S_R}{R^2}$. If the channel length increases to $2L$, the resistance of the channel will change to $2R$, and the noise power will change to $2S_R$ because the noise power of

each section of length L is S_R and the noise of each section is uncorrelated. The normalized noise power is $\frac{2S_R}{(2R)^2} = \frac{S_R}{2R^2}$. Thus, increasing the length of the channel decreases the normalized noise power. Equation 4.65 and 4.66 also show that the normalized noise power is inversely proportional to the channel length ($S_n \propto \frac{1}{L}$). In Figure 45, the length of the accumulation region of the channel decreases with increasing drain-source voltage due to the pinch off point shifting away from the drain to the source region ($\frac{1}{L} \propto V_{ds}$). Therefore, S_n increases slightly with V_{ds}, as shown in Figure 52. Figure 53 shows that the experimental results for the normalized noise power versus the drain-source voltage when different gate voltages are applied.

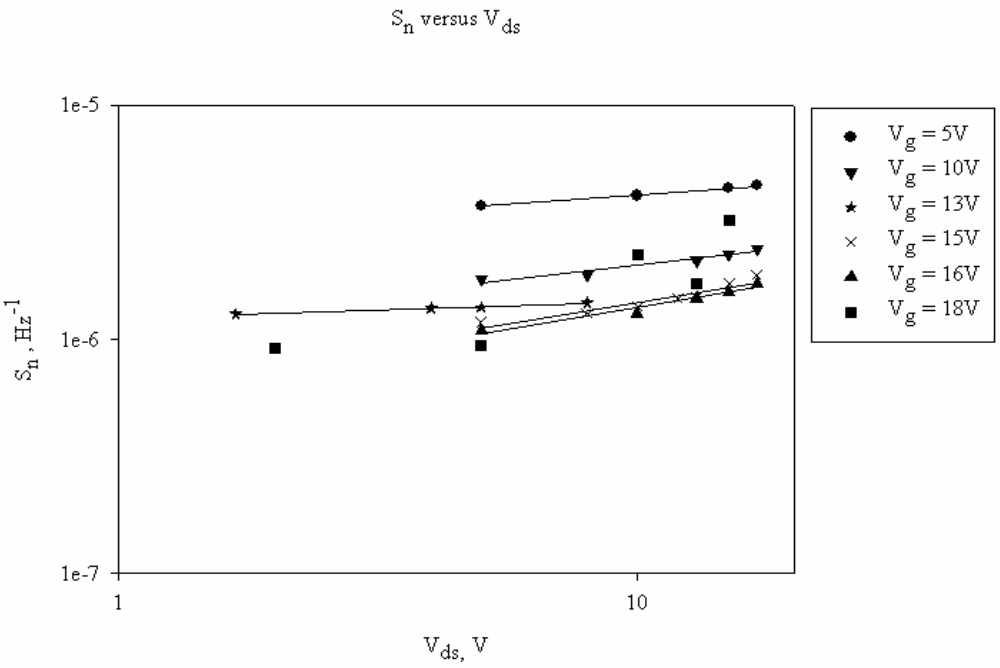

Figure 52 Simulation results S_n versus V_{ds} for different V_g (simulated times from 20μs to 31μs).

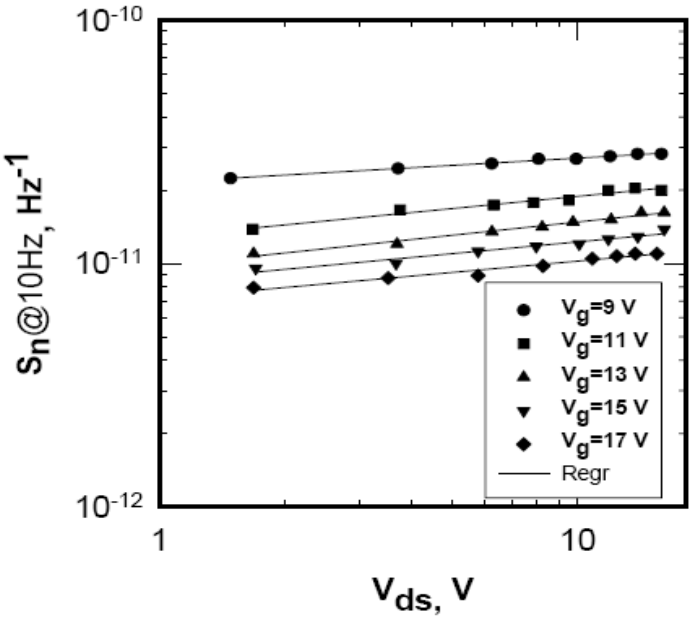

Figure 53 Experimental results S_n versus V_{ds} for different V_g [7].

As shown in Figure 52 and 53, the magnitudes of S_n from the simulation results are much larger than the experimental results because I used $\alpha = 1$ and frequency equals 1Hz to calculate the magnitudes of S_n. α_H was calculated using the values of the free charge densities in the previous experiments, and calculation results gave α_H was 1×10^{-3} [21]. To match the simulation results with the experimental results, the value of α_H would be 10^{-4}.

S_n is defined as

$$S_n(f) = \frac{\alpha_H}{fN}$$

where the number of carriers in the channel is $N = C_g WL(V_g - V_t)/q$; therefore,

$$S_n(f) = \frac{\alpha_H q}{fC_g WL(V_g - V_t)} \tag{5.2}$$

Equation 5.2 shows that α_H does not change the slopes of the curves on the log-log plot. When $V_{ds} = 15V$, the simulation result shows $S_n \propto V_{ds}^{0.32}$. When $V_{ds} = 15V$, the experimental result shows $S_n \propto V_{ds}^{0.18}$.

5.3 The Effect of Drain-Source Current on Noise Power Spectra

The relation between the normalized noise power and the drain-source current is investigated in this section. Figure 54 shows the magnitude of the normalized noise power versus the drain-source current for different gate voltages (5V, 10V, 13V, 15V, 16V, 18V). The same data was used in the previous section. In this section the plots are created according to the drain-source current instead of the drain-source voltage. Equation 5.2 shows that the normalized noise power is inversely proportional to the channel length ($S_n \propto \frac{1}{L_{effectivechannel}}$). The length of the accumulation region of the channel decreases due to the pinch off point shifts away from the drain to the source region, and the resistance of the accumulation region of the channel also decreases. The resistance of the accumulation region of the channel R_n limits the flow of the drain-source current. I_{ds} increases with decreasing R_n. Thus, the effective channel length decreases as I_{ds} increases in the saturated region ($I_{ds} \propto \frac{1}{L_{effectivechannel}}$), as shown in Figure 55.

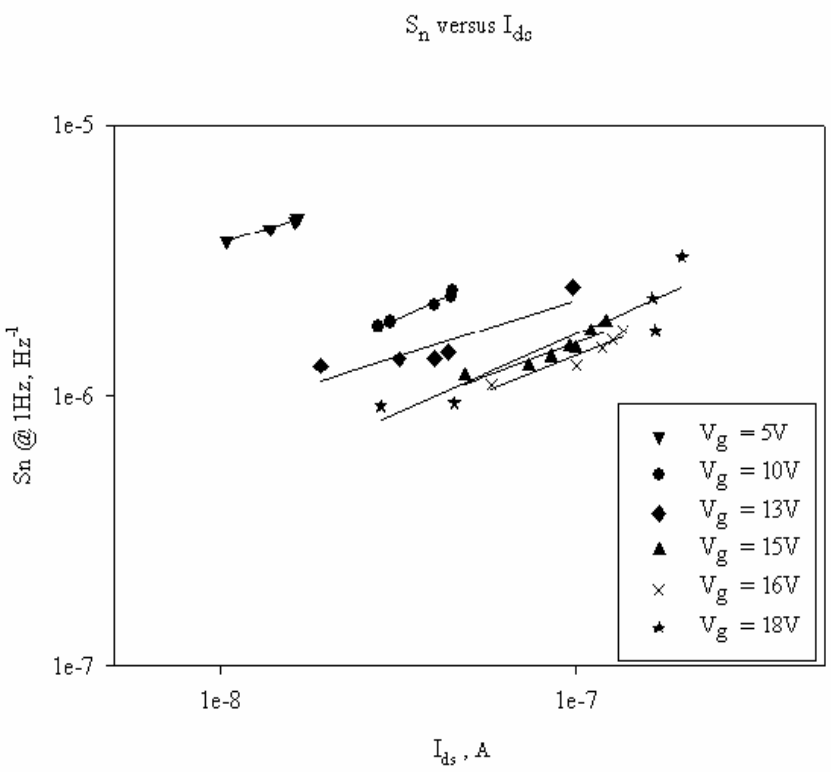

Figure 54 Simulation results S_n versus I_{ds} (simulated times range from 20μs to 31μs).

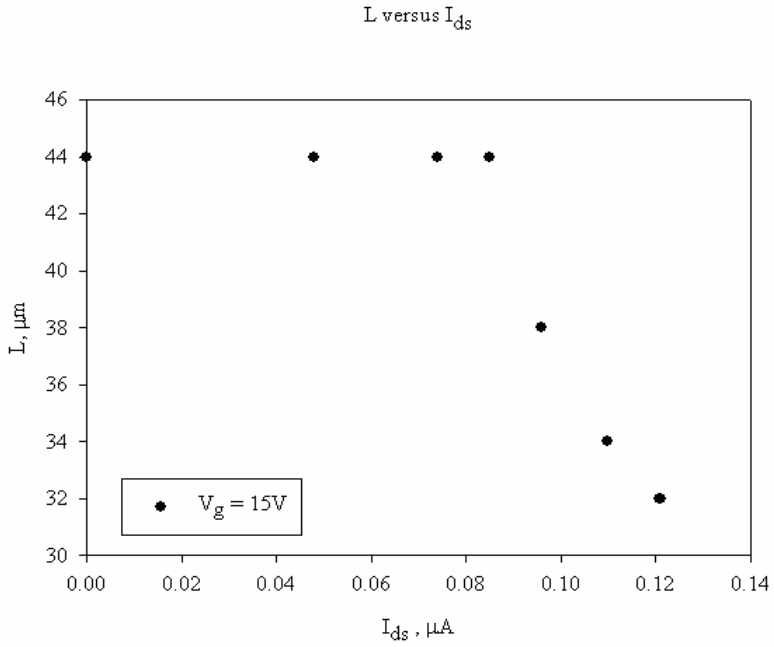

Figure 55 The effective channel length with the drain-source current when $V_g = 15\text{V}$ (simulated times range from 8.3μs to 27μs).

I expect that the normalized noise power is proportional to the drain-source current in the saturated region ($S_n \propto I_{ds}$). Figure 54 shows that the simulation results of the normalized noise power versus the drain-source current when different gate voltages are applied (5V, 10V, 13V, 15V, 16V, 18V). As shown in Figure 54, the normalized noise power increases with increasing drain-source current ($S_n \propto I_{ds}$). And Figure 56 shows the experimental results. The magnitude of I_{ds} and S_n from the simulation results are different from the experimental results. As I explained in the previous section, the difference is due to the electron drift mobility, Hooge's parameter α_H and frequency.

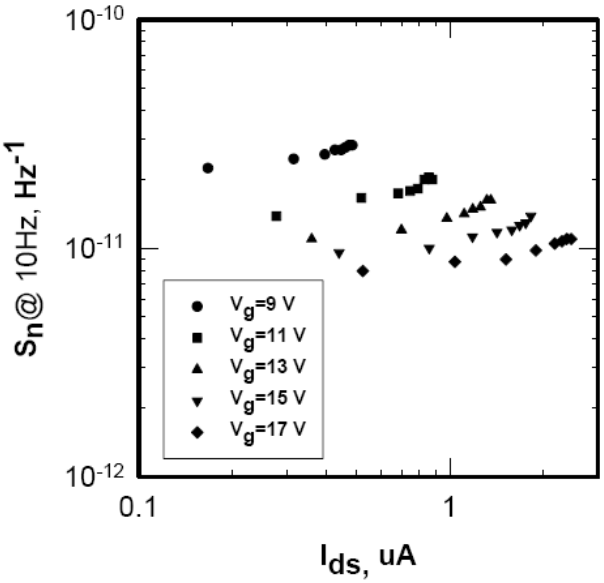

Figure 56 Experiment results S_n versus I_{ds} for different V_g [7].

5.4 The Effect of Gate Voltage on Noise Power Spectra

Figure 57 shows the simulation results of the normalized noise power versus the inverse of the gate voltage. S_n is measured for different V_{ds} (5V, 10V, 13V, 15V, 17V). Let us consider one of the curves from Figure 49 ($V_{ds} = 5V$) which shows that I_{ds} increases with V_g ($I_{ds} \propto V_g$).

The charge densities in the channel (N) increases with V_g ($N \propto V_g$). If $1/f$ noise is caused by N independent carriers, and each carrier generates $1/f$ noise, then the total noise power spectrum (S_{GN}) due to N carriers is $S_{GN} = NS_{1N}$, where S_{1N} is the noise power generated by one carrier. In the same way, the total noise power spectrum generated by $2N$ independent carriers is $S_{G2N} = 2NS_{1N}$. As I described in the previous chapter, the normalized noise due to N carriers is $S_{nN} = \frac{S_{GN}}{G_N^2} = \frac{NS_{1N}}{G_N^2}$, and the normalized noise due to $2N$ carriers is $S_{n2N} = \frac{S_{G2N}}{G_{2N}^2} = \frac{2NS_{1N}}{(2G_N)^2} = \frac{NS_{1N}}{2G_N^2} = \frac{1}{2}S_{nN}$. Therefore, doubling the number of carriers halves the normalized noise ($S_n \propto \frac{1}{N}$). I expect that the normalized noise power is inversely proportional to the gate voltage ($S_n \propto \frac{1}{V_g}$). Figure 57 shows that the simulation results match with the prediction.

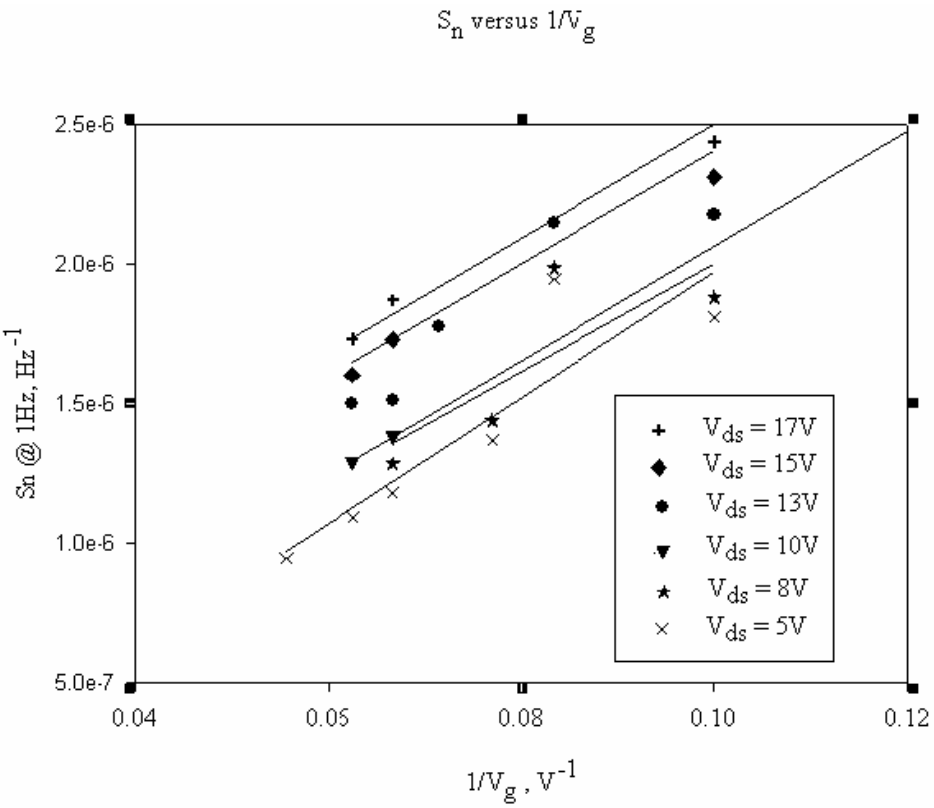

Figure 57 Simulation results S_n versus $1/V_g$ for different V_{ds} (simulated times range from 20μs to 25μs).

6. CONCLUSIONS AND FUTURE WORK

The objective of this work was to understand the measured results in a-Si:H TFTs from previous studies and in particular to test hypotheses put forward by Mr. Kim to explain the observed dependence on gate voltage, length and drain-source voltage. The objective was achieved by simulating the operation of the a-Si:H TFT using three main equations (Poisson's equation, the current equation and the continuity equation). The low frequency noise in a-Si:H TFTs can be calculated using the simulation results and compared to the experimental results.

Matlab was used to numerically simulate the operation of the a-Si:H TFTs. Computation time is important in simulations. Running time for each equation was recorded and compared. Significantly more time was spent solving Poisson equation compare to the other equations. Therefore, different methods of solving Poisson's equation were tested: the finite element method (FEM), the Gauss-Seidel method (GS), Jacobi's method, and the successive over-relaxation (SOR) method. In comparison among these methods, the SOR method used minimum time. The 2-D Poisson's equation solver (SOR method) was explained in detail including the initial conditions and the boundary conditions. Verification of the code was achieved by comparing with an analytical solution.

In the thesis, I presented 2-D simulation results, and a study of the low frequency noise in hydrogenated amorphous silicon thin film transistors. The simulation results show that the magnitude of the drain-source current increases with the drain-source voltage and increasing the gate voltage leads to a nonlinear increase in the magnitude of the drain-source current. The simulation results also show that the square root of the magnitude of the drain-source current and the gate voltage satisfy the equation $I_{ds} = \frac{\mu C_i W}{2L}(V_g - V_{th})^2$, and decreasing the effective channel length leads to increase of the magnitude of the drain-source current in the saturated region. The simulated drain-

source current is approximately a factor of 20 smaller than the experimental data. I believe that the magnitude of the electron drift mobility should have been 10 times larger than used in the simulation. However, the magnitude of the drift mobility should have only a minor effect on the charge distribution in the channel. Thus the noise calculation are not affected.

The magnitude of the normalized noise power can be calculated using the simulation results. The analysis results of the noise power show that the normalized noise power increases slightly with the drain-source voltage, and the magnitude of the normalized noise power is inversely proportional to the gate voltage which is an effect of the number of carriers in the channel. Doubling the number of carriers halves the normalized noise. The magnitude of the normalized noise power is also inversely proportional to the channel length which is an effect of the active volume. The magnitude of the normalized noise power agrees with the experimental data for a Hooge's parameter $\alpha_H = 1\times10^{-3}$. The experimentally determined Hooge's parameter α_H, calculated using the values of the free charge densities in the previous experiments, are in the range of $1\times10^{-3} - 2\times10^{-3}$ [21] in good agreement with the above value.

The low frequency noise in hydrogenated amorphous silicon thin film transistors might be due to generation-recombination noise and that type of noise is certainly present in a-Si. Since the simulated noise varies with applied voltages in a manner similar to the experiments, the noise in a-Si TFTs is consistent with the noise originating within the a-Si which was assumed in the noise calculations.

Although the results are in agreement with the hypothesis the noise in the TFTs originates with the noise in the a-Si:H, other noise sources might be in agreement with the experimental data. In particular, low frequency noise due to trapping at the interface or in the insulator should be considered in future work. Such a calculation would use the carrier density profile in the channel determined by my simulations. If differences exist between the two models, then the experimental data can be used to determine the origin of the noise in the a-Si:H TFTs.

REFERENCES

[1] S. O. Kasap, *Principles of Electrical Engineering Materials and Devices Revised Edition*, Boston: McGraw Hill, 2000.

[2] "http://www.varian.com/media/xray/products/pdf/Flat Panel Xray Imaging 11-11-04.pdf, pp.3", 2007.

[3] S. O. Kasap, *Handbook of Imaging Materials 2th Edition*, edited by A. S. Doamond and D. S Weiss, New York: Marcel Dekker, 2001.

[4] "http://www.iue.tuwien.ac.at/phd/hoessinger/img85.gif", 2008.

[5] "http://www.fys.ruu.nl/~vansark/pic/asih.gif", 2008.

[6] Webster E. Howard, *Thin-Film Transistors*, edited by Cherie R. Kagan and Paul Andry, New York: Marcel Dekker, 2003.

[7] Kang-Hyun Kim, M. Sc. Thesis, *Low Frequency Noise in Hydrogenated Amorphous Silicon Thin Film Transistors*, University of Saskatchewan, Saskatoon, Canada, 2006.

[8] H. Nyquist, "Thermal Agitation of Electric Charge in Conductors," *Physical Review*, vol 32, pp. 110-113, 1928.

[9] "http://www.utdallas.edu/~hellums/docs/EE7331/Fall2004/ShotNoise.pdf", 2004.

[10] "http://en.wikipedia.org/wiki/Autocorrelation", 2008.

[11] M. J. Buckingham, *Noise in Electronic Devices and Systems*, Market Cross House: Ellis Horwood, 1983.

[12] R. A. Street, *Hydrogenated Amorphous Silicon*, Cambridge: Cambridge University press, 1991.

[13] David W. Grave, *Field Effect Device and Applications*, New Jersey: Prentice Hall, 1998.

[14] Jin Jang, *Thin-Film Transistors*, edited by C. R. Kagan and Paul Andry, New York: Marcel Dekker, 2003.

[15] Martin J. Powell, "The Physics of Amorphous Silicon Thin Film Transistors", *IEEE Transactions on Electron Devices*, vol36, pp. 2753-2763, 1989.

[16] "http://mathdl.maa.org/mathDL/4/?pa=content&sa=viewDocument&nodeId=607&bodyId=963", 2007.

[17] "http://www.ece.uwaterloo.ca/~ece104/notes/ece104week4.ppt", 2007.

[18] William H. Press, Brain P. Flannery, Saul A. Teukolsky and William T. Vetterling, *Numerical Recipes in C*, Cambridge: University of Cambridge press, 1988.

[19] "http://mathworld.wolfram.com/FourierSineSeries.html", 2008.

[20] "http://www.springerlink.com/content/a244r3804qww224h/fulltext.pdf", 2008.

[21] R. E. Johanson, M. Gunes and S. O. Kasap, "Noise in hydrogenated amorphous silicon", *IEE Proceedings: Circuits, Devices and Systems*, 149, 68, 2002.